



Histocompositional organization and toughening mechanisms in antler



John G. Skedros^{a,b,*}, Kendra E. Keenan^a, David M.L. Cooper^c, Roy D. Bloebaum^{a,b}

^a Bone and Joint Research Laboratory, George E. Whalen Department of Veterans Affairs Medical Center, Salt Lake City, UT, USA

^b Department of Orthopaedic Surgery, University of Utah, Salt Lake City, UT, USA

^c Department of Anatomy and Cell Biology, University of Saskatchewan, Saskatoon, Saskatchewan, Canada

ARTICLE INFO

Article history:

Received 20 December 2013

Received in revised form 4 June 2014

Accepted 13 June 2014

Available online 22 June 2014

Keywords:

Deer antler

Collagen fiber orientation

Bone microstructure

Toughness

Osteons

Bone adaptation

ABSTRACT

Mechanical testing studies by Krauss et al. (2009) and Gupta et al. (2013) suggest that the extraordinary toughness of antler bone is primarily achieved by intrinsic/nanostructural mechanisms instead of extrinsic/microstructural mechanisms. However, this conclusion is based on data from extremely small specimens from one antler loaded only in tension, which impedes discernment of the relative importance of intrinsic vs. extrinsic mechanisms. In the present study we conducted analyses into the microstructural features of antler for details of potential additional microscale toughening characteristics, as suggested by recent mechanical testing studies of *bulk* specimens. The data are also considered in view of the above-mentioned studies concluding that extrinsic/microstructural toughening mechanisms are less important than nanoscale/intrinsic toughening mechanisms in antler. Mule deer antlers were evaluated using: (1) backscattered electron imaging for micro-mineralization, (2) circularly polarized light for osteonal interfacial complexity and collagen fiber orientation (CFO) heterogeneity, and (3) X-ray 3D micro-computed tomography for osteon/vessel orientation, density, and size. Results showed: (1) hyper-mineralized seams of approximately 3–4 microns thickness within relatively hypermineralized “zones” that course circuitously along osteonal interfaces, (2) highly heterogeneous CFO, including increased oblique-to-transverse CFO near/adjacent to osteon peripheries, and (3) osteons are often highly elongated in 2D. 3D reconstructions show that a considerable percentage of the vascular canals course obliquely with respect to the antler long axis. While results show multiple possible extrinsic-level histological characteristics in antler bone, it remains to be determined if microstructural characteristics become subsidiary to nanostructural characteristics in enhancing toughness during the majority of post-yield behavior of antler bone when loaded in a biologically relevant fashion.

Published by Elsevier Inc.

1. Introduction

Antler is considered bone because it is comprised of hydroxyapatite, collagen, non-collagenous proteins, water, and predominantly primary osteons (Bloebaum et al., 1997; Chapman, 1975; Currey, 2002; Gomez et al., 2013; Kierdorf et al., 2000; Krauss et al., 2011; Landete-Castillejos et al., 2007a; Launey et al., 2010b). The typical paucity of secondary osteons (Haversian systems) in antler (Gomez et al., 2013; Krauss et al., 2011) reflects the fact that nearly all species cast off these structures annually. They re-grow at a very fast rate with the majority of the growth being completed in just 3–4 months (Banks et al., 1968; Chapman, 1975), hence leaving insufficient time for the coupled

osteoclastic/osteoblastic remodeling process that forms traditional secondary osteons (Gomez et al., 2013; Krauss et al., 2011). Because antler breakage can significantly reduce reproductive success (Clutton-Brock, 1982), natural selection favors resilient/tough tissue that can withstand higher impact loads, bending moments, and torsion seen frequently in the male-to-male combat of the rutting (mating) season. Elk antler has been shown to have the highest strain to failure of all bones studied, with an ultimate tensile strain of ~12%, which is six times higher than the ultimate tensile strain of human cortical bone (~2%) (Currey, 2002). In this perspective it is notable that in compression tests of bulk specimens of North American elk antler, Kulin et al. (2011) reported that their specimens often did not break even at 25% strain.

The seminal work of Currey (1979, 1984, 1990) suggested that the extraordinary toughness of antler is strongly influenced by its relatively low mineral content, which reduces its material stiffness and is somehow coupled with mechanisms that enhance its

* Corresponding author at: 5323 South Woodrow Street, Suite 200, Salt Lake City, Utah 84107, USA. Fax: +1 801 747 1023.

E-mail address: jskedrosmd@uosmd.com (J.G. Skedros).

capacity to develop microdamage without catastrophic failure (i.e. fracture). Subsequent studies revealed microcracking behavior associated with microstructural features of the tissue but detailed analysis of antler microstructure was not pursued in these studies (Vashishth, 2004; Vashishth et al., 2003; Zioupos and Currey, 1994; Zioupos et al., 1994).

In a recent set of elegant studies, Krauss et al. (2009) and Gupta et al. (2013) reported experimental data suggesting a very unusual toughening mechanism present in antler that has not been identified as being prominent in human or bovine bone. Based on changes in small-angle X-ray diffraction patterns (SAXD) that occurred while progressively loading (in tension) matchstick-like specimens (16 mm × 400 μm × 200 μm) from antlers of Iberian elk (red deer) (*Cervus elaphus hispanicus*)¹, they drew fundamentally important conclusions: (1) this mechanism is at the collagen fibrillar (nanoscale) level of the antler material, and (2) it not only begins during pre-yield loading but dominates during post-yield loading. Therefore, they emphasized that this *nanoscale* toughening mechanism is unusual primarily because it is more important and effective than *microscale* mechanisms that dominate in human and bovine bone. This is a significant distinction because, while suggested toughening mechanisms in bone occur across the spectrum from nanostructure to microstructure, the most important of these have typically been considered to be at the *microstructural* level, especially during post-yield deformation as shown in the more highly mineralized “typical” bones that have been studied (Barth et al., 2010; Ciarelli et al., 2009; Dong et al., 2011; Koester et al., 2008; Launey et al., 2010b; Skedros et al., 2005; Zimmermann et al., 2009; Zioupos and Currey, 1994). Gupta, Krauss and co-workers’ emphasis on the dominance and time course (i.e. starting in the pre-yield/post-yield transition) of nanostructural toughening mechanisms is a revolutionary idea in bone biomechanics and, therefore, has important implications for understanding intricacies of the structural biology and mechanical behavior of other natural mineralized composite materials in the contexts of normal, aged, and disease states.

By contrast, mechanical tests conducted by Launey et al. (2010b) and Kulin et al. (2011) provide clear evidence that *microstructural* toughening mechanisms are at work – and prominently so – in North American elk antler. For example, Launey et al. (2010b) utilized real-time (in-situ) videography during environmental SEM imaging to view microcrack propagation during bending tests in specimens with much greater tissue volume (specimen size: 12 mm × 3 mm × 2.0–2.5 mm) than those of Krauss et al. (2009) and Gupta et al. (2013). Analysis of these bulk specimens revealed at the peripheries of the primary osteons the presence of “hypermineralized regions” (below we call these “zones”, and there is a hypermineralized “seam”, or “cement line”, contained within the “zone”) that help ramify and disperse developing microcracks, thus helping to avoid fracture by absorbing energy and reducing stress concentrations. Nevertheless they also argued that *intrinsic* toughening mechanisms dominate during plastic deformation. This conclusion in microcrack propagation tests in bending contrasts with findings of Kulin et al. (2011) who found that, in their bulk specimens of North American elk antler (6 mm × 4 mm × 4 mm) tested in compression, the primary osteons and their interfaces are the

dominant loci for the extrinsic mechanisms that enhance both pre- and post-yield toughness. Notably, when compared to the prior studies of antler mechanical properties the experiments of Kulin et al. (2011) more closely mirror natural conditions because they tested their specimens using strain rates that more likely resemble those produced by combat loads.

Despite these insights the four landmark studies that have reported data supporting and/or stimulating discussions of these important ideas in bone biomechanics and structural biology are based on experiments conducted on only one antler in each study ($n = 3$) (Gupta et al., 2013; Krauss et al., 2009; Kulin et al., 2011; Launey et al., 2010b). Nevertheless, in these studies of antler biomechanics an important duality has emerged in devising comprehensive mechanical tests of this tissue – nanostructural and microstructural toughening characteristics and mechanisms must be studied to determine the extent that both are present and their relative importance. This distinction is based on important toughening mechanisms in bone that are, respectively, either “intrinsic” (ahead of a crack tip and <1 μm in scale and largely material independent) or “extrinsic” (behind a crack tip and >1 μm in scale and largely material dependent) (see Appendix 1). The importance of microcracking extrinsically is that it results in both microcrack bridging and deflection, which are the most potent toughening mechanisms shown in bone (at least in non-antler bone) and have been shown to typically involve osteonal structures and/or other microstructural interfaces (Dong et al., 2011; Hoo et al., 2011; Koester et al., 2008; Launey et al., 2010a; Ritchie et al., 2005).

As noted above, and in contrast to these studies of antler specimens in bending and tension (Gupta et al., 2013; Krauss et al., 2009; Launey et al., 2010b), Kulin et al. (2011) found a more important role for osteon-level characteristics in toughening, as shown by their compression tests at high strains (up to 25%) and multiple strain rates (10^{-3} , 10 , 10^3). Although scanning electron microscopy of fracture paths showed that, as expected, failure of antler occurs at multiple scales of its hierarchical organization, from macrostructure to nanostructure, the involvement of microstructural characteristics seemed preeminent in the data of Kulin and co-workers. For example, splitting and sliding between osteons, with localized osteon buckling was observed in transversely loaded specimens. By contrast, splitting and tearing of osteons was observed in longitudinally tested specimens. They concluded that large plastic deformations are:

... attributed to the reduced mineral content [of antler] relative to long bones that allows the osteons to deform more easily, as well as (and perhaps more importantly) the irregular shape of the osteons. The irregular osteon shape leads to mechanical “interlocking” between osteons, and increases the load necessary for slipping between osteons to occur. This is supported by microstructural observations indicating failure tends to propagate between osteons, but is occasionally forced through osteons due this interlocking. (pg. 1038).

In addition, they found that during bulk deformation the tissue exhibited shearing along osteonal boundaries at approximately a 45-degree angles, resembling microstructural/extrinsic-based failure mechanisms in secondary osteonal bone in human long bones (Ebacher et al., 2007). In fact, previous studies have shown that shear deformation in oblique orientations (cross-hatched microcracks) is the major mechanism of the post-yield deformation of human cortical bone in compression (Ebacher et al., 2007; Leng et al., 2009). Because these findings show the relative importance of extrinsic mechanisms in compression tests of antler, they contrast with the emphasis on intrinsic failure mechanisms gleaned from the tension tests of Krauss et al. (2009) and Gupta et al. (2013). Placing heavy emphasis on one of these mechanisms

¹ North American elk are *Cervus elaphus canadensis* and are less commonly referred to as wapiti. In Europe there are many subspecies of *Cervus elaphus* and these are considered “red deer”. In North America the moniker “red deer” is not used to describe elk, hence in this study we use “elk”, not “red deer”, to describe all subspecies of *Cervus elaphus*. For the purpose of this study we refer to red deer as “elk” in order to remain consistent with common usage of “elk” in North America and because this usage: (1) is also consistent with recent studies of North American elk antlers (Kulin et al., 2011; Launey et al., 2010b) that are heavily referenced in the present investigation, and (2) helps to avoid additional confusion that can result from the fact that the species referred to as “elk” in Europe are called “moose” in North America (<http://en.wikipedia.org/wiki/Deer>) (Nowak, 1999).

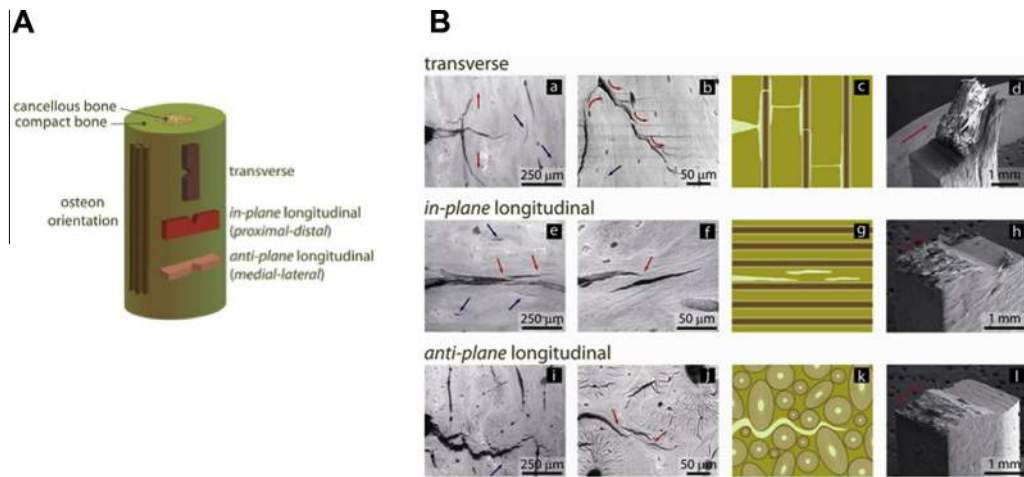


Fig. 1. (A) Illustrations of the machined specimens and their orientations within the elk antler ($n = 1$) tested by Launey et al. (2010b). Note that the osteon orientation is diagrammatically represented as being predominantly longitudinal. (B) Images from Launey et al. (2010b) showing mechanisms for stable crack propagation and toughening in the transverse and longitudinal orientations of compact bone of an elk antler. Backscattered electron images of stable crack growth during *in situ* R-curve testing in the (a, b) transverse, (e, f) in-plane longitudinal, and (i, j) anti-plane longitudinal orientations. SEM fractography images and (c, g, k) schematics of the crack trajectory for each orientation. In the transverse direction (a–d), the prominent toughening mechanisms are in-plane crack deflection and out-of-plane crack twisting. In the longitudinal orientation (both in-plane and anti-plane), the dominating toughening mechanism is ‘uncracked-ligament’ bridging (e, f, j). The red arrows indicate the direction of deflection in (a), twists in (b), crack propagation in (d, h, l), and uncracked-ligament bridges in (e, f, j) involving two-dimensional uncracked regions along the crack path that can bridge the crack on opening (Yang et al., 2006). The blue (darker) arrows delineate microcracks that formed at the osteon/matrix interface along the axis of the bone (for enhanced detail see: 10.1016/j.actbio.2009.11.026). Such microcracking is essential for many of the toughening mechanisms in bone, notably crack bridging and crack deflection, which predominate at micrometer-scales and above. (Reprinted with permission of the authors and Elsevier Inc.).

(intrinsic vs. extrinsic) likely reflects the different failure mechanisms in these strain modes as well as other aspects of the loading regimens used. It is also important to emphasize that Gupta, Krauss and co-workers’ contrasting findings of the ‘dominance of intrafibrillar plasticity through mineral/collagen sliding’ were based on tension tests of match-stick-like antler specimens, while the toughness during tension failure tests of *bulk* specimens of typical secondary osteonal bone is mainly a function of *extrinsic* mechanisms (typically involving osteonal structures and interlamellar interfaces) (Currey, 2002; Martin et al., 1998; Skedros et al., 2013).

In previous studies, we have suggested that the hypermineralized seams in antler are functionally analogous to the hyper-mineralized cement lines (also “seams” or “sheaths”) that surround traditional secondary osteons (these are also known as “reversal lines”) (Skedros, 1995; Skedros et al., 2005). As prominent sites for microcracking, both cement lines and hypermineralized seams have strong implications for fracture behavior. For example, secondary osteons affect the mechanical properties of limb bones by contributing to their resistance to failure (so-called “toughening”) because developing microcracks generally are deflected by cement lines instead of crossing them (Donahue and Galley, 2006; Norman and Wang, 1997; O’Brien et al., 2005a; Wasserman et al., 2008; Zimmermann et al., 2009). Although several toughening mechanisms have been proposed for cortical bone (Barth et al., 2010; Gupta et al., 2006a; Peterlik et al., 2006), microdamage deflection at cement lines is one of the most important (Koester et al., 2008; Launey et al., 2010a; Martin et al., 1998; O’Brien et al., 2007; Skedros et al., 2005) and the potential interaction of this mechanism with intrinsic/intrafibrillar failure mechanisms cannot be detected unless the size of the tested specimens is sufficient to study both mechanisms.

Although the real-time μ XCT images taken by Launey et al. (2010b) during bending tests of bulk elk antler specimens illustrate prominent/specific extrinsic microcracking along the hyper-mineralized seams with associated microcrack bridging, especially during in-plane and out-of-plane longitudinal loading, the gray-level contrasts in these images are so subtle that some readers might find

them unconvincing (Fig. 1).² It is plausible that the consequences of a similarly important microstructural toughening mechanism could not be detected by Krauss et al. (2009) and Gupta et al. (2013) because their specimens were very thin in cross section ($400 \mu\text{m} \times 200 \mu\text{m}$) and the SAXD analysis window was small ($200 \mu\text{m}$). Krauss et al. (2009) also implied that because their antler specimens had predominantly longitudinal collagen fiber orientation (CFO) (stated as unpublished observations; see also Fig. 1A), heterogeneity of this characteristic is not an independent toughening mechanism. By contrast, our previous histological observations of Rocky Mountain mule deer antler (*Odocoileus hemionus hemionus*) revealed microstructural characteristics that at that time had not been recognized as possibly important toughening mechanisms: (1) distinct hyper-mineralized seams (which we called “hyper-mineralized lamellae”) at the peripheral interfaces of primary osteons that resemble cement lines of human secondary osteons (Haversian systems), which were clearly evident in our high-contrast backscattered electron (BSE) images (Skedros, 1995), and (2) highly heterogeneous CFO and irregular osteon shapes were clearly evident in our circularly polarized light (CPL) images (unpublished observations) (Skedros, 1995).

From these perspectives, the present study examines the microstructure of antler bone for evidence of the potential microstructural/extrinsic toughening mechanisms that are at play to relative degrees in secondary osteonal bone in the limbs of many mammals. We also suggest possible reasons why Krauss et al. (2009) and Gupta et al. (2013) and Launey et al. (2010b) emphasize intrinsic mechanisms for antler failure, which contrasts with the implications of our histomorphological data. We also discuss the results of Kulin et al. (2011) that, while consistent with mechanical

² The principal investigator of the present study (JGS) has observed an unpublished microscopic video of a mechanical test of a bulk specimen from the study of Launey et al. (2010b), which was made in the laboratory of their co-author R.O. Ritchie. This video more convincingly shows how the rather subtle hyper-mineralized seams in the anti-plane longitudinal images in Fig. 1 disperse a microcrack into an array of smaller cracks that course into these hyper-mineralized regions. This video was presented by Dr. J. McKittrick in 2009 at the 8th Pacific Rim Conference on Ceramic and Glass Technology (Vancouver, British Columbia, Canada).

implications of our data, are also limited because of the small sample size ($n = 1$), questionable storage conditions of the antler, and unusual testing methods. Finally, we explore the mechanical implications of our histomorphological data in view of prior mechanical and histological studies of thin specimens of bovine fibrolamellar bone (Benecke et al., 2009; Gupta et al., 2006a, 2005).

2. Methods

Antlers were obtained from 11 adult male Rocky Mountain mule deer (*Odocoileus hemionus hemionus*; age range: 2–3 years) during a hunting season in late October in Northern Utah, USA. Gross examination of the carcasses of the animals showed no pathologies or reduced body mass. Additionally, the antlers were obtained from animals in a region where the prior winter and other climatic conditions were not unusual, hence nutritional deficiencies that can perturb normal antler histocomposition and biomechanical properties were not present (Landete-Castillejos et al., 2007b, 2012, 2010). The antlers were from complete and undamaged pairs with two deep tines on each side. Selection of this antler size as being fully representative of antler structure and histology that is designed for combat is supported by observations that two-year-old deer spar primarily with larger deer (Hirth, 1977). All of the animals and antlers were of approximately the same size. The antlers were obtained within 48 h after killing of the animals. The antlers showed no evidence of external periosteal “velvet”, indicating that they were mature.

Two 10 mm thick segments were cut transversely from each antler (i.e., from one side of each pair) starting at four centimeters

distal to the bifurcation as shown in Fig. 2. The bulk mineral content was determined by ashing two fragments (dried and defatted) from the cortex of the proximal segment (Skedros et al., 1993b). An average ash content (expressed as a percentage) was determined from these two values. All imaging (see below) was done in the cortical specimens taken adjacent to the ashed tissue. The cortical region was analyzed in this study because it is considered to be the most important for the mechanical properties of the overall antler structure (Currey, 2002; Currey et al., 2009).

Specimen fragments were then obtained from the transversely cut distal segment and were embedded in polymethyl methacrylate (PMMA) (Emmanuel et al., 1987). These embedded fragments had been placed adjacent to one another in order to form a single aggregate of specimens, which allowed all BSE imaging to be done in one calibrated session (Vajda et al., 1998). The specimen aggregate was then embedded into a well that had been machined into a block of Plexiglas®.

Using a low speed, diamond blade saw (Exact, West Germany) and continuous water irrigation, two 1.0 mm-thick transverse sections were obtained from the block of specimens (one was used for BSE imaging and the other for circularly polarized light (CPL) analysis) (Skedros et al., 2011). One surface of each of these thin sections was milled (EcoMet 250, Grinder Polisher; Buehler, Lake Bluff, Illinois, USA) and then mounted with PMMA onto a glass slide and the opposite side was milled to achieve 75 μm thickness.

2.1. Circularly polarized light (CPL) analysis in entire images

One of the milled sections was analyzed for collagen fiber orientation (CFO) variations using CPL according to the method of Boyde and Riggs (1990), where the specimens were viewed in the light microscope after being placed between appropriately crossed left- and right-hand polarizing filters (HNCP37 X 0.030 inch (0.762 mm) filter; Polaroid Corporation, Norwood, MA) (Neville, 1980; Skedros et al., 1996). Four 10 \times images (2048 \times 1536 pixels; approximately 1.1 mm \times 0.8 mm) were selected for analysis in each specimen. Variations in CFO were quantified in each image in terms of corresponding variations in the transmitted light intensity (based on the relative intensity of birefringence), where darker gray levels represent relatively more longitudinal CFO and brighter gray levels represent relatively more oblique-to-transverse CFO (Boyde and Riggs, 1990; Bromage et al., 2003).

The methods used to determine predominant CFO from the weighted mean gray level (WMGL) of each image have been described elsewhere (Bloebaum et al., 1997; Skedros et al., 1996). These methods include the elimination of the lower (darker) 20 gray-level values (i.e., 0, 1, 2, ... 19) that represent tissue voids such as vascular canals and lacunae. Variations in image gray levels are referred to as differences in “CFO/WMGL” (Skedros et al., 2011).

2.2. CFO heterogeneity in entire images

CFO heterogeneity is expressed as the sum of the full width at one-half of the maximum (FWHM) of the peak of the gray-level profile that was obtained from pixel histograms from each CPL image. This is similar to what is done to express the heterogeneity of micro-mineralization and other matrix parameters in human bone (Boskey, 2001; Ruffoni et al., 2007). Examples of CFO heterogeneity from entire CPL images were also obtained from thin transverse sections (75 μm) of mammalian limb bones used in prior studies (Skedros et al., 1999, 2009, 2011). These images were obtained from mature animals or individuals: mule deer calcaneus, equine radius, equine third metacarpal, and human femur (45 years-old Caucasian male who died from trauma). The non-human sections were obtained from the mid-shaft of the bones, and the human femoral section was obtained from the proximal

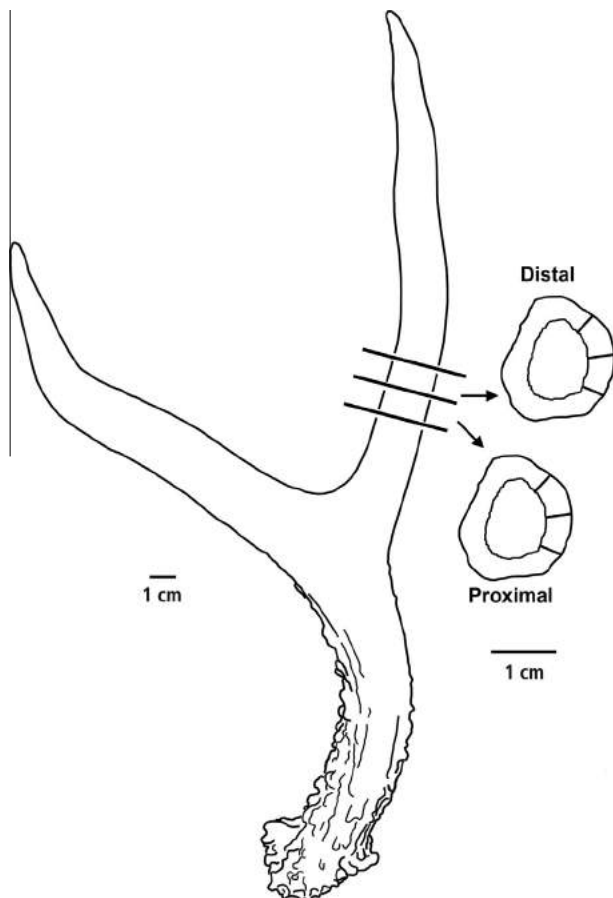


Fig. 2. Drawing of one of the antlers showing the sections and locations used for ashing (proximal segment) and imaging (distal segment). Anterior is to the left.

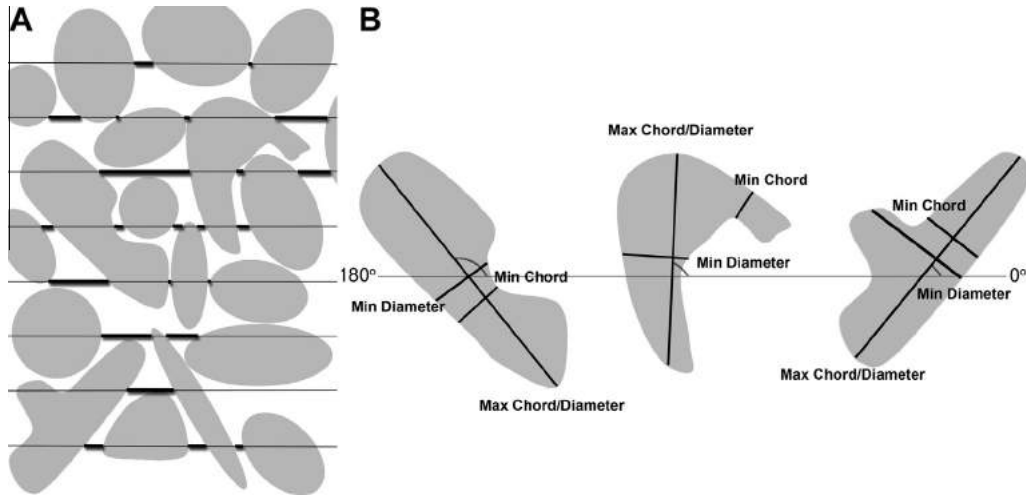


Fig.3. Schematic diagram showing how some of the histological parameters were measured. The thick black lines in (A) represent how interface distances were measured. (B) Shows how maximum and minimum diameter and chord lengths were measured as well as maximum chord angles (indicated by the curved lines). The lighter horizontal line that spans across all three osteons provides a point of reference for the maximum chord angle.

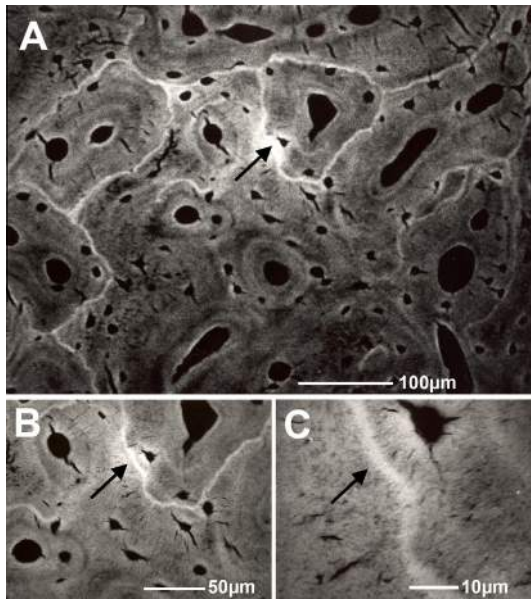


Fig.4. Backscattered electron (BSE) images of mule deer antler at various magnifications. The “bleached” area (i.e., whiter than surrounding bone) in the central portion of the low magnification image is the result of damage caused by the electron beam that occurred while obtaining the higher magnification images. This artifact is a consequence of repeated scanning in one location (Bloebaum et al., 2005; Holmes et al., 2000) that is common when imaging is done for illustrating the same location at multiple magnifications; this was avoided in the quantitative analysis because the sequential scanning is not needed. Magnifications: (A) 200×; (B) 500× and (C) 2000×. The specimen is fully calcified and unstained, and was embedded in polymethyl methacrylate. Note that the 2000× image is only used for illustration purposes. 1500× images were used for the quantitative analysis as described in the Methods section.

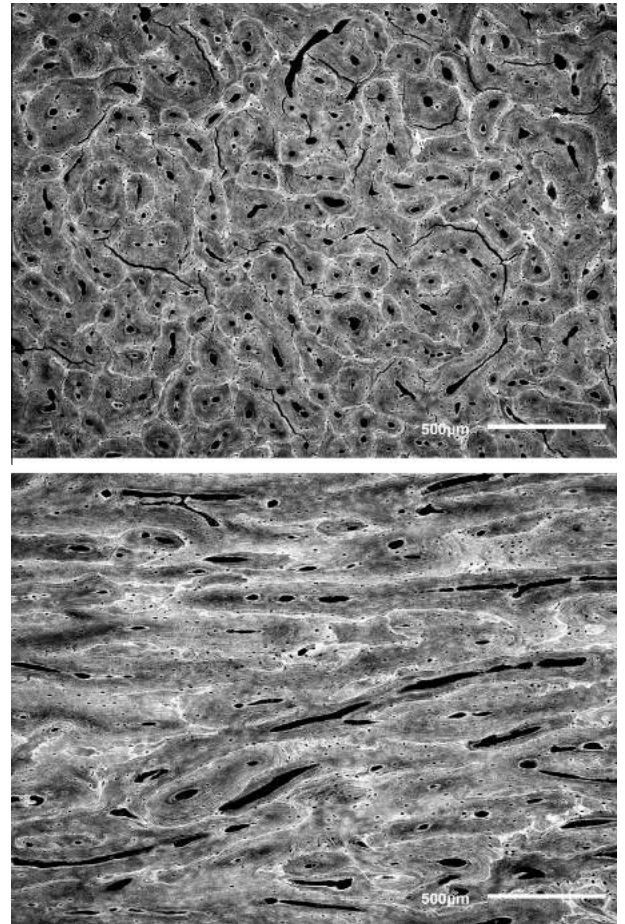


Fig.5. Backscattered electron (BSE) images of the same mule antler specimen obtained at 50× in both transverse (Top) and longitudinal (Bottom) views. The long axis of the antler beam courses from left-to-right in the image at the bottom. Hypermineralized seams/zones are visible at the periphery of the osteons (which are typically primary osteons). These 50× images were obtained using the same imaging conditions during the same imaging session. The specimen is fully calcified and unstained, and was embedded in polymethyl methacrylate.

shaft. These bones were selected because they span a range of habitual load complexity, from relatively simple (deer calcanei) to complex (equine third metacarpal and human proximal femur) with osteonal and/or matrix adaptations that correlate with this habitual complexity, as described previously (Skedros, 2012).

2.3. Distance between osteon interfaces

Using the antler CPL images, the distances between the interfaces in the bone microstructure were measured (using the Straight Line Tool in ImageJ; version 1.43; [Rasband \(1997–2009\)](#)) along eight equidistant parallel lines that were randomly oriented on each image ([Fig. 3A](#)). The distances between adjacent interfaces were averaged to obtain a mean distance between interfaces in each image.

2.4. Osteon geometry measurements

Geometry data were obtained from each osteonal structure ($n = 810$ total osteons) using ImageJ. The periphery of each osteon was traced using the Wand Tracing Tool and subsequently the Fit Spline function was used to more accurately contour the osteon tracing. Then the Measure function was used to quantify total area (including the area of the osteon's canal(s)), perimeter, maximum and minimum chords, maximum chord angle, and circularity index (where 1.0 = perfect circle). The osteon maximum and minimum

diameters were determined using the Straight Line Tool in ImageJ. In addition to circularity index, two measures of osteon elongation (based on chord and diameter aspect ratios) were used to estimate the potential obliquity of the three-dimensional orientation of each osteonal structure. This allowed for the possibility of detecting the presence of osteon shapes (e.g., undulating shapes) that might be missed when using only diameters ([Fig. 3B](#)). Elongation based on diameters is expressed as the ratio of the maximum diameter to the orthogonal diameter (designated as “minimum”) at the one-half of the maximum diameter. Circular osteons have maximum:minimum diameter and chord ratios equal to 1, and elongation increased this value. If osteons are circular, then this suggests that they are preferentially oriented along the long axis of the antler, in accordance with the diagrammatic depiction in [Fig. 1A](#).

In order to compare data from the primary osteonal structures of antlers to the secondary osteons of other species, osteon cross-sectional morphology data were obtained from complete secondary osteons (Haversian systems) that were measured in previous studies of CPL images from thin transverse sections of diaphyseal cortices of mature bones from four species: deer calcanei ($n = 7$),

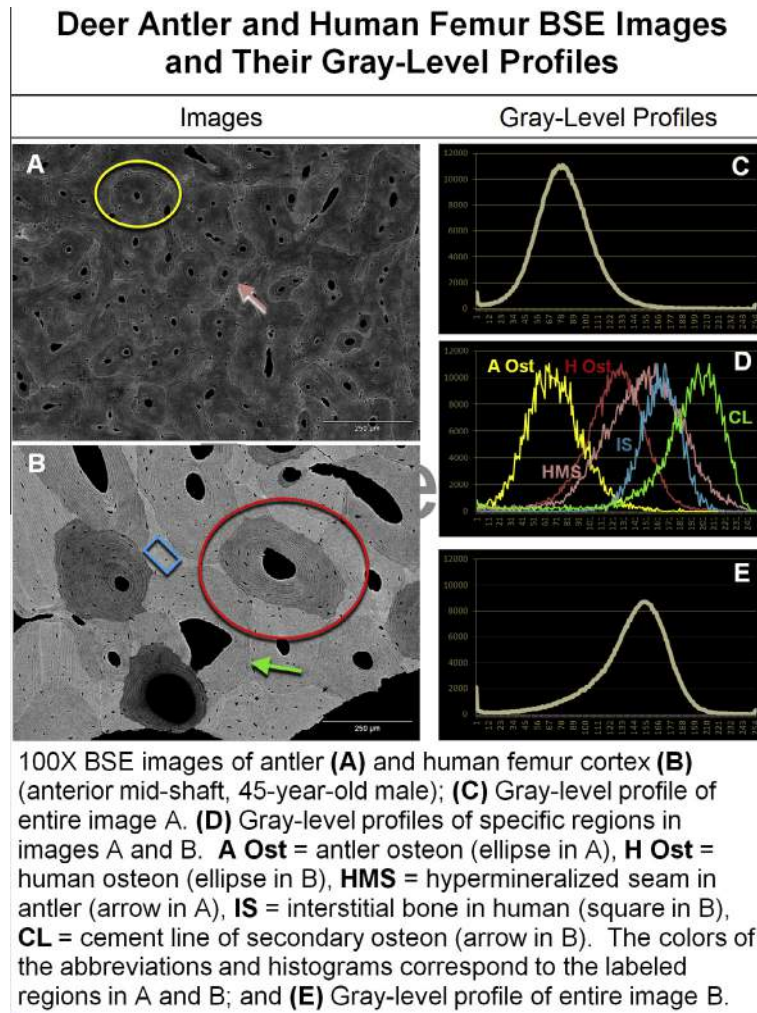


Fig. 6. Backscattered electron (BSE) 100 \times images of antler and human bone taken under the same imaging conditions. Gray-level profiles (of entire images A and B) are shown at right (top right is antler, bottom right is human). In the middle image at the right are gray-level profiles of the pixels in the specific regions shown in the two images. Note that the hypermineralized seam (HMS) in the antler has a mineralization level that resembles that of the region of human interstitial (IS) bone. These images were obtained using the same imaging conditions during the same imaging session. However, in contrast to the consistent small size of the ROIs used in the quantitative analysis of BSE images in this study (see Methods section), the ROI sizes vary considerably for the specific purposes of this illustration only. Although the sizes of these ROIs vary in this illustration, the gray-level profiles are consistent with the profiles obtained when using smaller/standardized ROIs in the same regions (data not shown). The specimens are fully calcified and unstained, and were embedded in polymethyl methacrylate. Normalization of the profiles was done in accordance with methods of ([Boyce et al., 1990](#)).

sheep tibiae ($n = 7$), equine third metacarpals ($n = 7$), and human femora ($n = 12$) (Skedros et al., 1999, 2009, 2012). These data were obtained from the entire samples, and one specimen per species was obtained for the CFO heterogeneity analysis described above. In order to illustrate CFO heterogeneity, an equine radius was used instead of the sheep tibia because of the generally relatively lower secondary osteon population density of the latter bone.

2.5. Osteon morphotype scoring

Two independent evaluators assessed images of each of the individual osteons, which were digitally cropped out of each antler CPL image. Each osteon was scored using the following “morphotyping” scheme: (1) relatively dark birefringence (longitudinal CFO) across the entire osteon wall, (2) relatively bright birefringence (transverse-to-oblique CFO) within the inner half (near the vascular canal) of the osteon wall with relatively dark birefringence within the peripheral half of the osteon wall, (3) relatively dark birefringence within the inner half of the osteon wall with relatively bright birefringence within the peripheral half (near the peripheral interface) of the osteon wall, (4) bright birefringence within both the inner one-third of the wall and the peripheral one-third of the wall with relatively dark birefringence within the middle one-third of the wall, and (5) bright birefringent patterns of CFO traversing the majority of the osteon wall. This scheme is similar to the osteon morphotype scores that have been

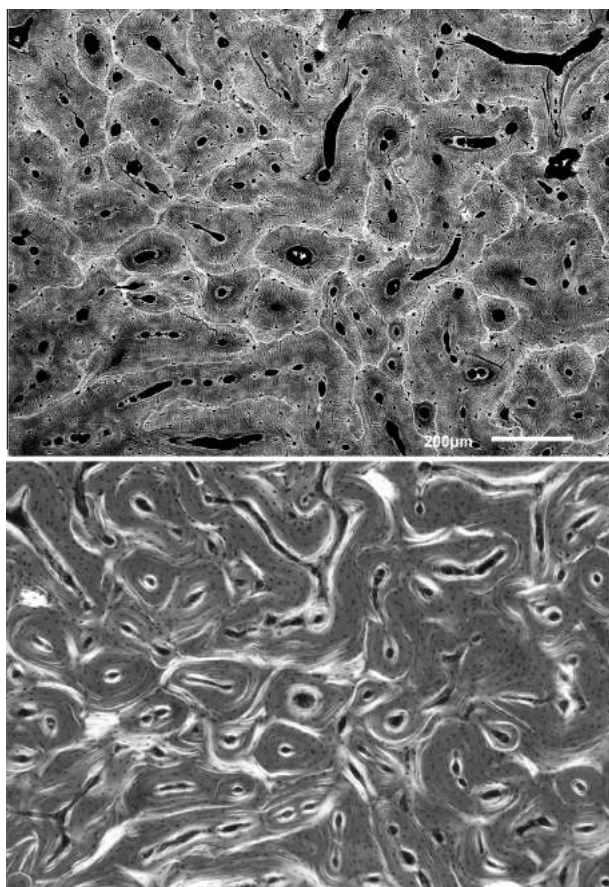


Fig. 7. Two images of antler from the same field of view: one BSE (Top) and one CPL (Bottom). These images show that the hypermineralized seams at periphery of the osteons are often within regions where the collagen is orientated more oblique-to-transverse when compared to the more longitudinal collagen in the majority of the osteonal wall. The specimens are fully calcified and unstained, and were embedded in polymethyl methacrylate. The specimen used for this illustration was ground and polished to a final thickness of 20 μm .

described previously by Skedros et al. (2009) in secondary osteons of various species. The brighter birefringence within the walls of the antler osteonal structures was often “patchy” or incomplete, which resembled the incomplete “hoops” or other “hybrid” CFO patterns that are seen in some secondary osteons (Skedros et al., 2011). The bright birefringence that traverses the majority of the osteonal wall resembles bright/alternating CFO patterns that are seen in some secondary osteons (Beraudi et al., 2010; Skedros et al., 2011).

2.6. Backscattered electron (BSE) image analysis

A thin section taken adjacent to each section used for the CPL analysis was then coated with a thin layer of carbon (conductive coating). The carbon-coated specimens were then imaged in one imaging session using a JEOL 6100 Scanning Electron Microscope (JEOL USA, Peabody, MA, U.S.A.) with a backscattered electron (BSE) detector (Tetra, Oxford Instruments, Buckinghamshire, U.K.). Consistent operating conditions were maintained, including voltage (20 kV), probe current (0.7 ± 0.02 nA), aperture (50 μm), and working distance (15 mm). Fluctuations in probe current were adjusted after image capture (Bloebaum et al., 2004, 1997). A calibrated, digitized BSE image (1500 \times) was obtained from regions that included the periphery and the adjacent bone of each of three randomly selected osteonal structures that were initially viewed at 50 \times . Therefore, there were three 1500 \times images/antler specimen (six images from each antler). Random selection of the osteons was facilitated with a random number generator and a grid that was superimposed over each image as described in Skedros et al. (2005). When viewing the 1500 \times images, bright seams were obvious at the interfaces of the osteonal structures. Relative differences in the mineralization of these bright seams and the adjacent bone on both sides of the bright seam were quantified, and were expressed as corresponding differences in their WMGLs. The analysis regions of interest (ROIs) were equal in size, including those analyzed in a human femur (see below). In accordance with methods of Skedros et al. (2005), the ROIs were 0.7 μm in diameter (6 pixel diameter) in the 1500 \times images. In contrast to the CPL images where WMGL corresponds with CFO, WMGL in BSE images corresponds with the level of mineralization (Skedros et al., 1993a,b). The adjacent bone that appeared to fall in a more recognizable osteon was considered ‘osteon bone’ and the other adjacent region was considered ‘bone of the trabecular scaffold’. This allowed for distinguishing more subtle mineral heterogeneity that might occur across osteonal peripheries as reported in secondary osteons of human bone (Skedros et al., 2005).

2.7. Mineralization heterogeneity in BSE images

For comparative purposes, BSE image analyses were also conducted on a specimen obtained from the anterior aspect of the transversely sectioned mid-shaft of an adult human femur. This specimen was representative of the specimens used in our previous study of secondary osteon cement line mineralization (Skedros et al., 2005). Examples of microscopic mineralization heterogeneity and CFO heterogeneity in antler were also obtained from representative BSE and CPL images of the same location from one antler. This heterogeneity is represented by histogram profiles of the gray-level values from these images.

2.8. X-ray micro-computed tomography (micro-CT)

The methods used to obtain the 3D micro-CT reconstructed images of the osteonal canals have been described previously (Cooper et al., 2003). Each specimen was imaged in a Skyscan™ 1172 scanner (Bruker Micro-CT, Kontich, Belgium) at 78 kVp and

Table 1A
Summary of osteon/microstructure data.

	Max chord length (μm)	Max diameter (μm)	Chord AR (Max:Min)	Diameter AR (Max:Min)	Interface distance (μm)	Osteon area ($\text{mm}^2 \times 10^{-3}$)	Percent osteonal area	Circularity index	Max chord angle ($^\circ$)
<i>Present Study</i> (35 images)									
Mean	202.7	199.3	1.7	2.1	97.5	0.018	80.3	0.71	88
Std Dev	91.2	88.8	0.5	1.2	63.8	0.015	5.5	0.16	55
Range (min–max)	(56.0–583.3)	(51.9–563.8)	(1.1–4.1)	(1.0–11.4)	(5.8–409.4)	(0.002–0.088)	(70.0–90.0)	(0.23–0.96)	(0.15–179.9)
<i>Krauss et al.</i> (One image)									
Mean	221.4	210.7	1.6	2.0	123.6	0.022	77.2	0.75	82
Std Dev	114.9	113.0	0.4	1.0	52.4	0.019		0.17	58
Range (min–max)	(75.0–1003.7)	(56.9–998.6)	(1.1–3.6)	(1.0–8.5)	(22.3–309.9)	(0.002–0.178)		(0.27–0.98)	(1.2–179.8)
<i>Chen et al.</i> (One image)									
Mean	240.7	230.8	1.6	1.8	131.2	0.029	79.6	0.79	89
Std Dev	122.6	120.0	0.5	0.9	87.1	0.023		0.15	49
Range (min–max)	(77.8–543.9)	(73.1–529.0)	(1.1–4.1)	(1.0–5.5)	(11.1–320.2)	(0.003–0.097)		(0.37–0.97)	(5.8–179)
<i>Launey et al.</i> (One image)									
Mean	295.7	254.1	1.7	1.4	137.9	0.038	74.4	0.75	67
Std Dev	178.1	135.6	0.5	0.4	107.0	0.036		0.19	47
Range (min–max)	(94.0–752.3)	(88.6–590.0)	(1.2–2.6)	(1.0–2.1)	(12.7–402.5)	(0.005–0.138)		(0.37–0.926)	(8.5–168)

AR = aspect ratio = maximum/minimum diameter or maximum/minimum chord.

Elongation based on diameters is expressed as the ratio of the maximum diameter to the orthogonal diameter at the one-half of the maximum diameter. Circular osteons had diameter and chord ratios close to 1, and elongation increases this value. If osteons are circular, then this suggests that they are oriented along the long axis of the antler, in accordance with the diagrammatic depiction in Fig. 1A.

Table 1B

Percentage of osteons with varying aspect ratios (ARs) in 2D images (based on maximum/minimum chord ratios).

No. osteons measured	Present study <i>n</i> = 810	Krauss et al. <i>n</i> = 192	Chen et al. <i>n</i> = 85	Launey et al. <i>n</i> = 11
AR between 1 and 1.5	39%	45%	54%	46%
AR between 1.5 and 2	41%	35%	31%	27%
AR between 2 and 3	18%	19%	12%	27%
AR > 3	2%	1%	1%	0%
AR > 1.4*	72%	68%	59%	91%

Elongation based on chords is expressed as the ratio of the maximum chord to the orthogonal minimum chord at approximately one-half of the maximum chord. Circular osteons had diameter and chord ratios equal to 1, and elongation increased this value. If osteons are circular/cylindrical, then this suggests that they are oriented along the long axis of the antler, in accordance with the diagrammatic depiction in Fig. 1A.

* The maximum:minimum chord ratio of a cylinder tilted 45° is 1.4. Cylindrical osteons tilted >45° have max:min ratios > 1.4.

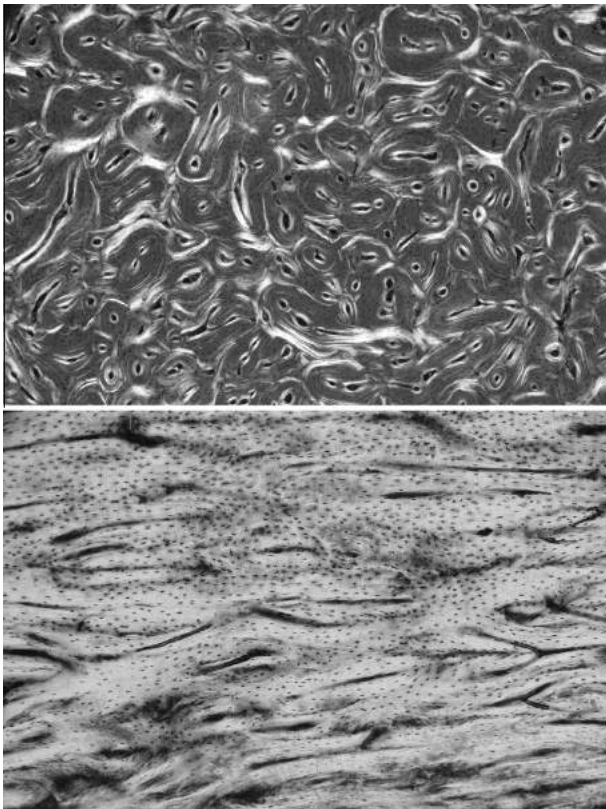


Fig. 8. Representative CPL images from the same antler specimen in both transverse (Top) and longitudinal (Bottom) views. In the top image there are some osteonal structures that are highly elongated even though the canals within them appear relatively less elongated (this was a frequent observation in this study). The osteonal structures also often have more than one canal. Multiple-canal osteons are considered “osteone conglomerates”. When compared to the image of the transverse section, the image of the longitudinal section image does not show the dramatic birefringence variations between the osteon periphery and the osteon wall. This suggests that the collagen at the osteon periphery is typically obliquely (not transversely) oriented; thus it appears relatively “bright” in both transverse and longitudinal views. The longitudinal collagen that appears darker in the transverse image is also brighter in the longitudinal image; this makes the image of the longitudinal section (Bottom) overall much brighter in CPL. The width of each image is 2.35 mm. These images were obtained using the same illumination and magnification. The specimens are fully calcified and unstained, and were embedded in polymethyl methacrylate.

125 μ A with a 0.5 mm aluminum filter. They were rotated through 180 degrees in 0.1 degree steps resulting in 1800 projections each involving 1.7 s exposures with 3-exposure averaging to improve signal to noise. The resulting datasets had an isotropic voxel size of 2 μ m³ (<5 μ m X-ray source spot size; 8.83 μ m camera (physical) pixel size).

One remaining portion from the distal segment of one antler was used for this analysis. Additionally, for comparisons with antler, the dorsal “compression” and plantar “tension” cortices (Su et al., 1999) of one mature deer calcaneus were examined. The dorsal cortex is expected to have relatively more uniformly longitudinal and less interconnected osteonal vascular canals and the plantar cortex is expected to have more irregularly oriented and more interconnected osteonal vascular canals. These variations presumably reflect histomorphology that enhances toughness where bone is weaker (i.e., in the habitual “tension” environment of the plantar cortex) (Skedros et al., 1997, 2001). By contrast, the antler osteonal vascular canals are expected to be even more irregularly oriented and more interconnected than the canals in these cortical regions in the calcaneus. These variations in the canal segments of the vascular network (which are contained within the osteonal structures) of each specimen were measured as the degree of anisotropy; this is calculated as one minus the ratio of the largest (1st) and smallest (3rd) Eigenvalues derived from a mean intercept length (MIL) analysis of the canals as generally based on Harrigan and Mann (1984) and described in detail in the Skyscan™ CT-analyzer user’s manual (August 1, 2009). The DA values can range from 0 (isotropic = no orientation) to 1 (anisotropic = oriented in one direction). Additional analyzed parameters included: (1) canal volume per total volume of bone (%), (2) canal separation (μ m), (3) canal diameter (μ m), and (4) canal number (1/mm).

2.9. Statistical analysis

Paired comparisons among the microscopic locations analyzed in the BSE images were assessed using Kruskal–Wallis multiple-comparison ANOVA (Hintze, 1995; Sokal and Rohlf, 1995). Spearman correlations were used to assess associations between CFO/WMGL and measures of 2D osteon elongation.

3. Results

The BSE image analyses clearly demonstrate the extensive presence of “bright lines” (referred to here as “hyper-mineralized seams”) (Fig. 4). These seams are approximately 3–4 microns (μ m) thick and they course circuitously through the bone at the peripheries of the more discernible osteons (>99.5% are primary osteons) or between interfaces formed by all other primary osteonal structures. These seams are also within relatively broader (~5–10 μ m) hypermineralized “zones” that are formed by the tissue immediately adjacent to the osteon interfaces. The BSE images also show that these bright seams/“zones” starkly contrast with the dark gray levels of the large majority of the antler tissue.

Results of the WMGL analysis in the BSE images confirm the observation that the seams are also invariably more highly mineralized than the adjacent osteonal bone ($p < 0.001$) and bone of the trabecular scaffold ($p < 0.001$). The means and (standard deviations) of these data are: hyper-mineralized seams 154.8 (17.7), intra-osteon bone beyond the “zone” 122.9 (21.1), and adjacent bone of the trabecular scaffold or osteonal bone beyond the “zone” 129.1 (20.4); here the higher numerical values indicate higher mineralization (Skedros et al., 2005). Mineralization levels (WMGLs) of the non-seam material (osteonal and/or bone of the

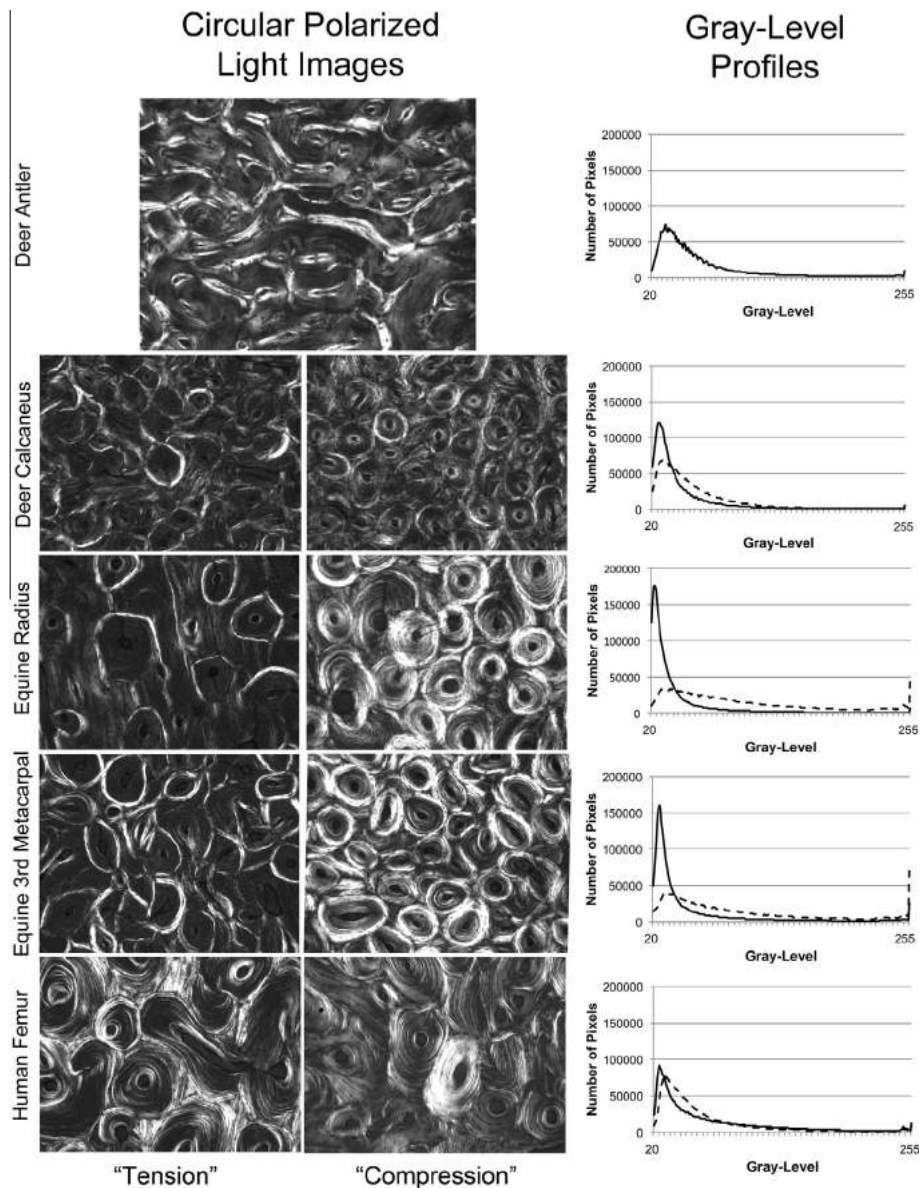


Fig. 9. Circularly polarized light (CPL) images and their CFO/gray-level profiles of an antler (at Top) and other mature bones from our previous studies: (1) dorsal “compression” cortex and plantar “tension” cortex of a deer calcaneus, (2) cranial “tension” cortex and caudal “compression” cortex of an equine radius, (3) dorsal-lateral “tension/shear” cortex and medial “compression” cortex of an equine third metacarpal, and (4) lateral “tension” cortex and medial “compression” cortex of a middle-aged human femur in the proximal shaft. The width of each image is 1.08 mm. The solid line in each graph at the far right corresponds with the image from the “tension region” and the dashed line corresponds with the image from the “compression region”. These images were obtained using the same illumination and magnification. The specimens are fully calcified and unstained, and were embedded in polymethyl methacrylate.

trabecular scaffold) are equivalent ($p > 0.5$). The mean and standard deviation for the ashed bulk specimens are 58.8% and 1.1%, respectively, which is consistent with data reported in studies of antlers in other species (Currey, 2002).

Fig. 5 shows two representative BSE images (one transverse and one longitudinal) that also demonstrate the presence of hypermineralized seams/zones. Fig. 6 shows BSE images and corresponding gray-level profiles (mineralization variations) of regions of interest in antler and femoral cortical bone from a healthy 45-years-old human male. Quantitative analysis of the gray-level contrasts in these images shows that the relatively highly mineralized interstitial bone of secondary osteons resembles the hyper-mineralized seams in the antler, suggesting that these regions have similar mineral content.

Fig. 7 shows a BSE image and a CPL image taken from the same field of view of a transversely sectioned antler. Examination of all

of the CPL and BSE images showed that there was occasionally one secondary osteon (Haversian system) per image, but this was a rare occurrence. Thirty-five images were quantified for this portion of the analysis. Eleven images from the original sample of 44 were not quantified due to damage (i.e., chipping and/or partial delamination) that occurred sporadically within the specimen during the milling process.

The morphology data obtained from primary osteons in the antler CPL images are summarized in Table 1A. Data from microscopic images of elk antler published in three prior studies are also listed for comparison. Table 1B shows results of estimates of osteonal obliquity based on 2D morphology of the images used in Table 1A.

Consistent observations of obvious variations in the intensities of birefringence throughout each CPL image, including in the vicinity of the osteonal interfaces and around the vascular canals are clearly seen in each image of transverse sections (Figs. 7 and 8),

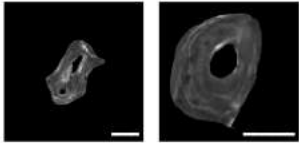
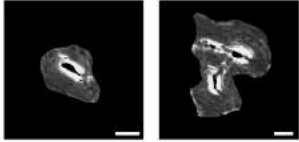
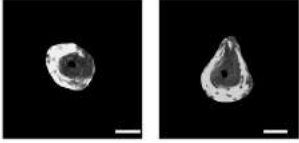
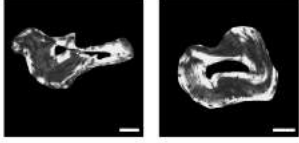
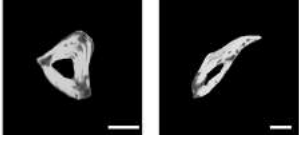
Morphotype Scores and Representative Images (510 Osteonal Structures Analyzed)		
Morphotype Score	Examples	Percent Prevalence
1		1.9%
2		15.9%
3		16.9%
4		53.8%
5		11.5%

Fig. 10. Results of osteon morphotype scoring with examples of each morphotype. The scale bar in each image is 50 μm .

but FWHM does not reflect these variations in distribution of birefringence. However, FWHM measurements obtained from the main gray-level peaks of representative antler CPL images are similar to regions in other bones that would be expected to have increased CFO heterogeneity (Fig. 9) as an adaptation for enhancing regional toughness in habitual compression. But the peaks are not substantially different between antler and these bone regions, suggesting that FWHM does not reveal all important details of the CFO variations.

Results of the correlation analysis showed a very weak relationship between the magnitude of osteonal elongation in 2D (expressed in terms of diameters and chords) and predominant CFO (expressed as WMGL) of the osteon wall ($r = 0.15$, $p < 0.05$). The results of the five-point scoring of each osteon (morphotype scores) in the antler CPL images are summarized in Fig. 10, and these data reveal additional details of potential extrinsic toughening mechanisms in antler. These data show that 54% of the osteons had type 4 morphology (i.e., bright birefringence within both the inner one-third of the wall and the peripheral one-third of the wall with a relatively darker birefringence within the middle one-third of the wall). In fact, 71% of the osteonal structures evaluated in this study had relatively longitudinal collagen in the majority of the osteon wall with highly oblique-to-transverse collagen at the osteonal interface (MTS 3 and 4), which is consistent with the CFO heterogeneity that has been proposed to be a toughening mechanism in secondary osteonal bone (Skedros et al., 2011, 2013).

CT scan images of the bulk specimen and region of interest of the antler specimen used in the 3D micro-CT reconstructions are shown in Fig. 11. High resolution 3D reconstructions of the

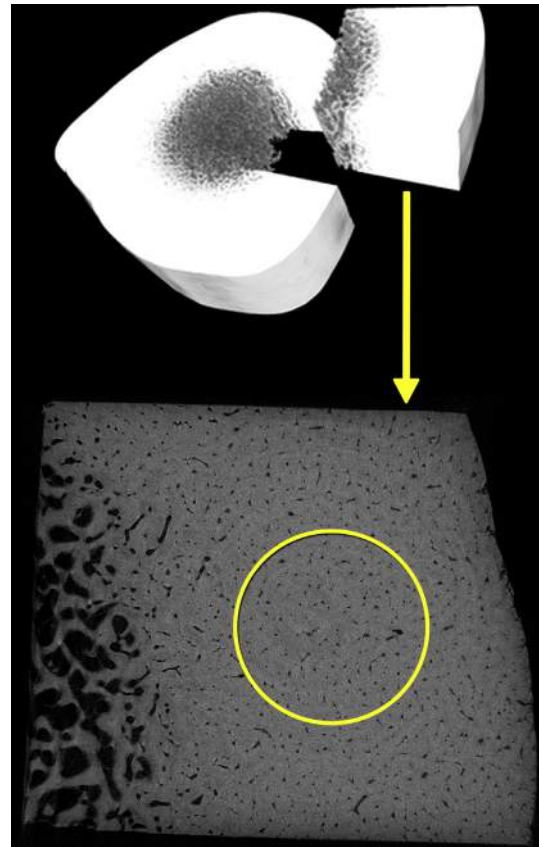


Fig. 11. CT scan images of the antler segment and the surface of the cylindrical volume of interest used to create the 3D reconstructions of the vascular canals in antler. The volume of interest was 1.9 mm diameter cylinder that was 0.95 mm long and was aligned along the long axis of the calcaneus or antler.

vascular networks of the antler and two calcaneus regions can be viewed using this internet link: [Web will be provided here.] These reconstructions allow for measurements of canal morphology to be made along the long axis of the antler or calcaneus. Quantitative analyses of these 3D reconstructions shows that the complexity of the vascular canals (e.g., the degree of tortuosity in their orientation and complexity of their inter-connections), which we thought would mirror the orientations of the osteonal structures (Figs. 7 and 8), were different than predicted (Fig. 12). (We predicted that the antler would have relatively more oblique orientations when compared to the dorsal and plantar calcaneus cortices.) Consequently, the percentage of the canals that are aligned within 20° of the long axis of the antler is likely much greater than expected (~55% for antler, ~50% for plantar calcaneus, ~57% for dorsal calcaneus). Antler has predominantly longitudinal orientation like the other specimens but, by contrast, has fewer transverse canals. In turn, antler had the highest degree of anisotropy of the three, which suggests more oblique branching of the vasculature than the other specimens. This is consistent with enhanced extrinsic/microstructural mechanisms that contribute to the greater toughness of antler.

The morphological data in Table 2 were obtained from secondary osteons of limb bones that have habitually non-uniform strain distributions (i.e., “compression”, “tension”, and “neutral axis” (high shear) regions. Comparing these data with those in Table 1 and show that the osteonal structures in antler are notably more elongated and irregularly shaped (i.e., lower circularity indices) ($p < 0.05$ of each characteristic in each antler vs. limb-bone comparison). Table 3 shows additional differences between antler osteons and general histomorphology and micro-mineralization

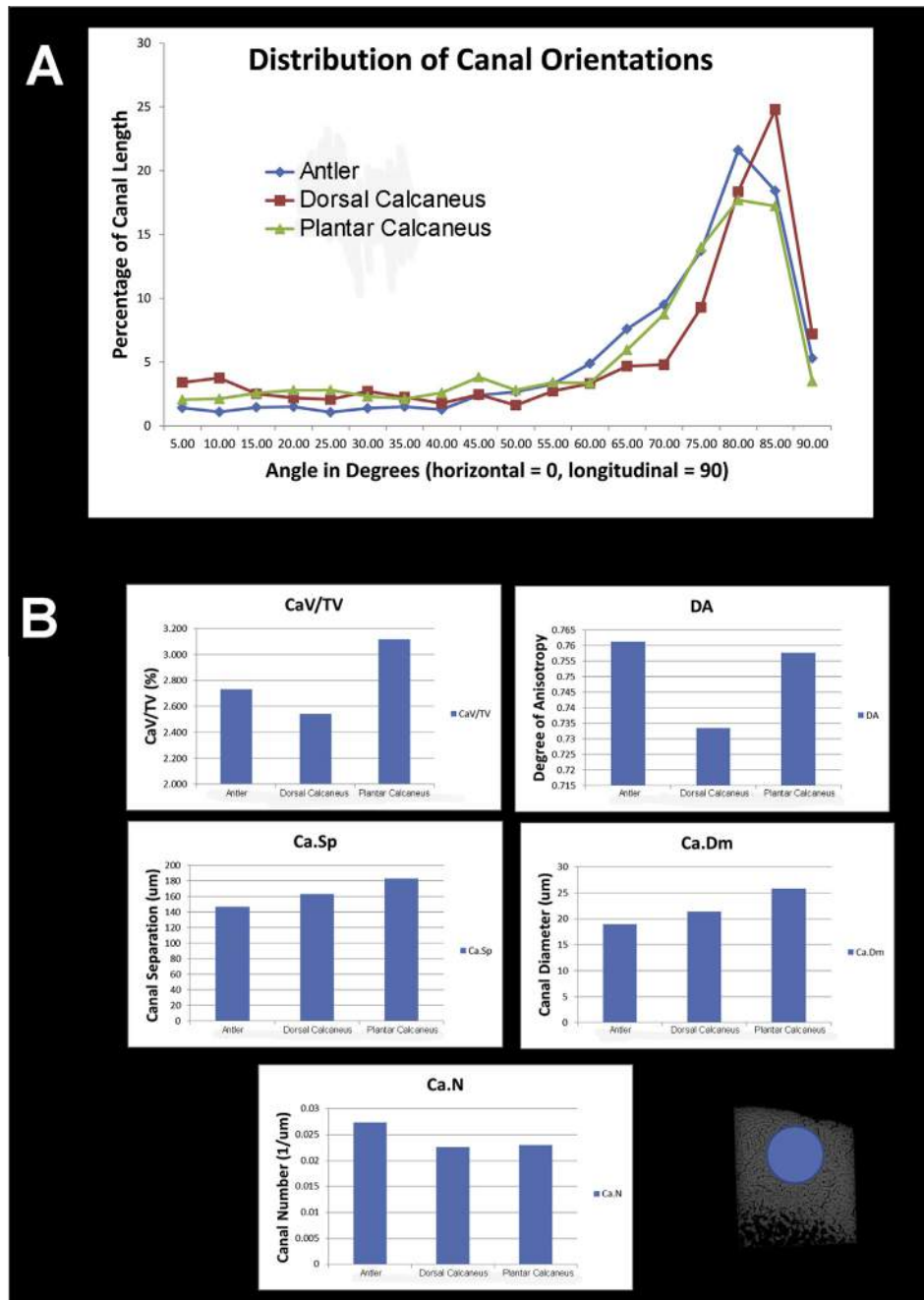


Fig.12. Quantitative analysis of the vascular patterns from the 3D reconstructed micro-CT images of antler, and dorsal and plantar cortices of a mature deer calcaneus. The volume of interest was 1.9 mm diameter cylinder that was 0.95 mm long and was aligned along the long axis of the bone or antler. (A) Histograms of the canal orientations, which were obtained after breaking the canal skeletons up into 25-pixel (47.5 μm) linear segments as described by Britz et al. (2012). (B) Vascular canal morphological data. These data show that the heterogeneity in vascular canal orientation is greatest in the plantar “tension” calcaneus cortex, intermediate in the antler, and least (i.e., canals are most longitudinal) in the dorsal “compression” calcaneus cortex. Based on our 2D osteon elongation data, it was predicted that the antler would show the greatest canal obliquity in 3D. The fact that antler canals are not as oblique/transverse as were predicted likely reflect correlations between canal and osteon orientations that are weaker than was anticipated (Fig. 7).

differences between antlers and various primate and non-primate limb bones used in our prior studies.

4. Discussion

This study shows that: (1) there are extensively distributed hyper-mineralized seams of approximately 3–4 microns thickness (Fig. 4) that are within relatively hypermineralized “zones” (or “regions” *sensu* Launey et al. (2010b) and Kulin et al. (2011)) that course circuitously along osteonal interfaces, (2) CFO is highly het-

erogeneous, including increased oblique-to-transverse CFO around canal lumens and often near/adjacent to osteon peripheries, and (3) the osteonal structures are often highly elongated in 2D images (Figs. 7 and 8). While the 3D reconstructed images generally confirm that a considerable percentage of the vascular canals course obliquely with respect to the long axis of the antler, the 2D data over-estimate the magnitude and relative percentage of the obliquity of osteon orientations (discussed below). In the 2D images, the antler osteonal structures are also notably more convoluted and tortuous than the secondary osteons in the plantar, med-

Table 2
Secondary osteon shape, maximum:minimum chord length, area, and population density in limb bones* [means and (standard deviations)].

Bone	Cortex	Shape	(Std)	%diff	M:M Chrd	(Std)	%diff	On.Ar	(Std)	%diff	N.On/Ar	(Std)	%diff
Deer calcaneus (n = 7)	Dorsal "C"	0.87	(0.08)		1.4	(0.2)		0.010	(0.011)		49.1	(5.1)	
	Plantar "T"	0.83	(0.10)	4% ^a	1.4	(0.3)	6%	0.016	(0.012)	34% ^b	37.8	(10.0)	30% ^b
	Med "S"	0.90	(0.05)		1.3	(0.2)		0.015	(0.008)		6.9	(3.6)	
	Lat "S"	0.89	(0.07)	2%	1.3	(0.2)	5%	0.019	(0.010)	17% ^a	6.5	(3.3)	6%
Sheep tibia (n = 7)	Cranial "S,T"	0.87	(0.09)		1.3	(0.2)		0.021	(0.020)		26.6	(11.1)	
	Caudal "S,C"	0.90	(0.04)	4%	1.3	(0.1)	4%	0.019	(0.013)	7%	1.2	(1.7)	>90% ^b
	Med "S"	0.92	(0.04)		1.3	(0.2)		0.020	(0.008)		0.9	(1.2)	
	Lat "S"	0.92	(0.04)	<1%	1.4	(0.2)	1%	0.023	(0.010)	16%	0.3	(0.5)	>90%
Horse 3rd metacarpal (n = 7)	Dorsal "T,S"	0.89	(0.10)		1.3	(0.2)		0.016	(0.009)		9.5	(5.2)	
	Plantar "C,S"	0.90	(0.10)	1%	1.3	(0.2)	0%	0.020	(0.010)	21% ^b	16.4	(6.9)	73% ^b
	Med "C"	0.91	(0.07)		1.3	(0.2)		0.023	(0.011)		17.1	(5.9)	
	Lat "T"	0.91	(0.07)	<1%	1.3	(0.2)	4%	0.023	(0.011)	1%	13.0	(7.2)	32% ^a
Human femur (n = 12)	Ant "T,S"	0.92	(0.04)		1.4	(0.2)		0.038	(0.017)		15.5	(5.2)	
	Post "C,S"	0.90	(0.06)	2% ^b	1.5	(0.3)	7% ^b	0.035	(0.017)	7%	14.9	(3.5)	4%
	Med "C"	0.93	(0.04)		1.3	(0.2)		0.041	(0.021)		15.8	(5.2)	
	Lat "T"	0.92	(0.05)	<1%	1.3	(0.2)	<1%	0.035	(0.018)	16% ^a	17.5	(4.3)	11%

* Shape = osteon circularity index (1.0 = perfect circle); (Std) = one standard deviation; M:M Chrd = osteon maximum:minimum chord length; On.Ar = osteon cross-sectional area ($\text{mm}^2 \times 10^{-3}$); N.On/Ar = secondary osteon population density (no./mm^2); %diff = % difference: anterior vs. posterior, or medial vs. lateral % difference is calculated using: $((\text{larger no.} - \text{smaller no.})/\text{smaller no.}) \times 100$; "T" = tension area, "C" = compression area, and "S" = shear area; Ant = anterior, Post = posterior, Med = medial, Lat = lateral.

^a $p \leq 0.05$.

^b $p \leq 0.01$.

ial, and lateral cortices of adult deer calcanei where it has been hypothesized that osteonal interfacial complexity enhances toughness for habitual tension and/or shear stresses of these regions (where enhanced histomorphological adaptations are expected because bone is weaker in tension and shear when compared to compression) (Skedros, 2012; Skedros et al., 2013). However, as discussed below, in antler the seemingly convoluted/tortuous appearance of the osteons in 2D can be difficult to interpret – 3D tortuosity can be only be determined by 3D reconstruction (Fig. 12).

In summary, these results show highly circuitous/convoluted primary osteonal interfaces in antler (compare osteon circularity indices in Tables 1–3) that are spatially coincident with predominantly oblique-to-transverse CFO and the hyper-mineralized seams/zones. This appears to provide microstructural interfacial complexity and modulus mismatch that seem ideal for resisting torsional and other complex stress conditions produced by variable loads of natural combat (Blob and Snelgrove, 2006; Clutton-Brock, 1982; Olvera et al., 2012). In view of biomechanical data showing that interfaces and matrix modifications within and between secondary osteons (rarely present in antler) correlate with enhanced extrinsic toughening in healthy/non-elderly secondary osteonal bone (Bigley et al., 2006; Hiller et al., 2003; Nalla et al., 2005a,b; O'Brien et al., 2005b; Yeni and Norman, 2000; Zimmermann et al., 2009), we argue below that all of these microstructural characteristics also contribute in an analogous way in enhancing extrinsic toughness in antler. In these contexts it is important to point out the difference in the formation process between the different osteon types (Table 3). Secondary osteons fill in an elongated cavity with a more or less circular outline eroded by an osteoclastic cutting cone. In contrast, the primary osteons in antler bone fill in (typically larger) intertrabecular spaces of more irregular shape that sometimes have become enlarged by osteoclastic resorption prior to infilling (Gomez et al., 2013; Kierdorf et al., 2013). This is why the primary osteons of antler are morphologically more complex (with often more than one vascular canal) and have a less orderly arrangement than secondary osteons. During antler histogenesis remnants of mineralized cartilage also can remain (Kierdorf et al., 2013; Landete-Castillejos et al., 2012), which could influence toughness. However, mineralized cartilage was not seen in the regions of the specimens evaluated in the present study.

An accepted idea in bone biomechanics is that the interactions of osteons with microdamage formation and propagation illuminate key aspects of how they enhance toughness. Strain and damage localization that characterize brittleness is avoided early on in the transition from elastic to inelastic behavior (Currey, 2002; Launey et al., 2010a). However, in antler this toughness must be accomplished without secondary osteonal remodeling because of the short growing phase that substantially limits this process from occurring (Gomez et al., 2013; Krauss et al., 2011). As a result, secondary osteons are rare in the locations we analyzed in the deer antlers (this is similar in elk (red deer) antlers (Gomez et al., 2013; Krauss et al., 2011)). Therefore, extrinsic/microstructural toughening is likely afforded by the hyper-mineralized interfaces of the primary osteonal bone. Because the hypermineralized seams and the hypermineralized "zones" wherein they reside are only rarely associated with typical secondary osteon remodeling in antler they seem more akin to resting lines that are laid down when primary osteons form (Gomez et al., 2013; Krauss et al., 2011; McKee and Nanci, 1996; Skedros et al., 2005). Consequently, the hyper-mineralized seams associated with these primary osteonal structures have been considered analogous, not developmentally homologous, to the hyper-mineralized cement lines (reversal lines) in secondary osteonal bone (Currey, 2002; Skedros et al., 2005). However, studies by Gomez et al. (2013) and Kierdorf et al. (2013) do show that in some cases the resorption of the trabecular scaffold of woven bone precedes the infilling of the intertrabecular spaces by primary osteons, and that hyper-mineralized ("bright") lines with a scalloped appearance along the borders of some primary osteons are present. This may indicate that these hypermineralized seams are actually more akin to reversal lines and hence may be developmentally homologous to cement lines in secondary osteonal bone.

In view of the observations of Kulin et al. (2011) and Launey et al. (2010b) (see footnote 2), the histomorphological data in the present study are also sufficiently compelling to suggest that antlers achieve microstructural modulus mismatch at the hypermineralized seams of the osteon interfaces similar to what is attributed to cement lines in secondary osteonal bone (Launey et al., 2010a; Olvera et al., 2012; Skedros et al., 2005). Although there is strong evidence that classical cement lines of secondary osteons are highly mineralized, it is possible that relative collagen deficiency accounts for the increased brightness of these lines and

Table 3
Histomorphology and regional composition of deer antlers (primary osteons) vs. secondary osteonal bone from limb bones of adult sheep, deer, horses, humans, and chimpanzees* (circular polarized light and BSE image analyses). The grayed rows indicate results from deer antler analysis.

Osteon size (cross-sectional area; $\text{mm}^2 \times 10^{-3}$)	Smallest in dorsal deer calcaneus (0.010 ± 0.011) [‡] 2nd smallest in medial deer calcaneus (0.015 ± 0.008) Largest in medial human femur (0.041 ± 0.021) Deer antler (0.018 ± 0.015)
Osteon shape (1.0 = perfect circle)	Most irregular (non-circular) in deer antler (0.71 ± 0.16) 2nd most irregular in plantar deer calcaneus (0.83 ± 0.10) Least irregular in medial human femur (0.93 ± 0.04)
Osteon elongation (maximum:minimum chord ratio)	Most elongated in deer antler (1.7 ± 0.5) 2nd most in posterior human femur (1.5 ± 0.2) Least elongated in several species (see Table 2) (1.3 ± 0.2)
Osteon population density (no./ mm^2)	Highest in dorsal deer calcaneus (49.1 ± 5.1) 2nd highest in plantar deer calcaneus (37.8 ± 10.0) Lowest in medial/lateral deer calcaneus (7.0 ± 3.5) Deer antler (primary osteons) (34.9 ± 5.1) [‡] Human femur (16.0 ± 4.6) (see Table 2)
Fractional area of osteonal bone (as the % of bone and vascular canal area)	Highest in deer antler (primary osteons) (80.3 ± 5.5) 2nd highest in equine plantar calcaneus (2nd osteons) (76.4 ± 3.5) Lowest in medial deer calcaneus (2nd osteons) (11.1 ± 6.6)
Regional heterogeneity in CFO (e.g., largest differences in CFO between the inner and outer aspects of an osteon vs. the majority of its wall)	Probably greatest in antler (This has not been quantified in a comparative analysis.)
Regional heterogeneity in mineralization (e.g., largest mineral content difference between the mid-osteonal wall and the 'cement line' region/zone)	Probably greatest in antler (This has not been quantified in a comparative analysis.)

*From Skedros et al. (2009, 2011 and 2013). Comparisons of osteon morphology (top three items above) are made using these regions of non-elderly adult bones with $\geq 50\%$ secondary osteonal bone per area: (1) calcanei from sheep, deer, and horses, (2) radii from sheep and horses, (3) cranial cortex of sheep tibiae (other cortical regions have few osteons), (4) third metacarpals (MC3s) from horses, and (5) femora from humans and chimpanzees.

*Although antler has lower OPD (of primary osteons) it has greater canal density than these regions of the calcaneus (see Fig. 12). This is because, unlike secondary osteons, primary osteons of antlers often have two or more canals (see Figs. 7 and 8).

[‡]Numbers in parentheses represent means \pm standard deviations.

CFO = collagen fiber orientation.

of the analogous hyper-mineralized seams that can be seen in the BSE images of our antlers (Gomez et al., 2013; Skedros et al., 2005).³

³ Although most prior studies that have published microscopic images of antler did not use techniques with sufficient contrast and resolution to reveal the hypermineralized seams (and hypermineralized "zones" within which the seams are located), there are a few that have demonstrated them in BSE images. The imaging with the best contrast and resolution, which resemble our BSE images, is that Krauss et al. (2011). Kierdorf and co-workers have published BSE images from the non-deciduous antler pedicle regions of elk (red deer) (Kierdorf et al., 2000) and roe deer (Kierdorf et al., 2013) that also show these contrasts vividly.

Antler fracture is minimized during combat loads (impact, torsion, bending, etc.) because energy absorption is enhanced by a propensity for microdamage formation and dispersion without extensive microdamage propagation and coalescence (Vashishth, 2004, 1997, 2002; Zioupos et al., 1994, 1996). However, this understanding of the micromechanical behavior of antler was initially determined in experiments that did not pursue details of the histological correlates of this behavior. An example of the incomplete understanding of interactions of antler histology with microdamage formation and propagation at the time when these and other notable seminal micromechanical studies were being conducted is illustrated by Zioupos et al. (1996):

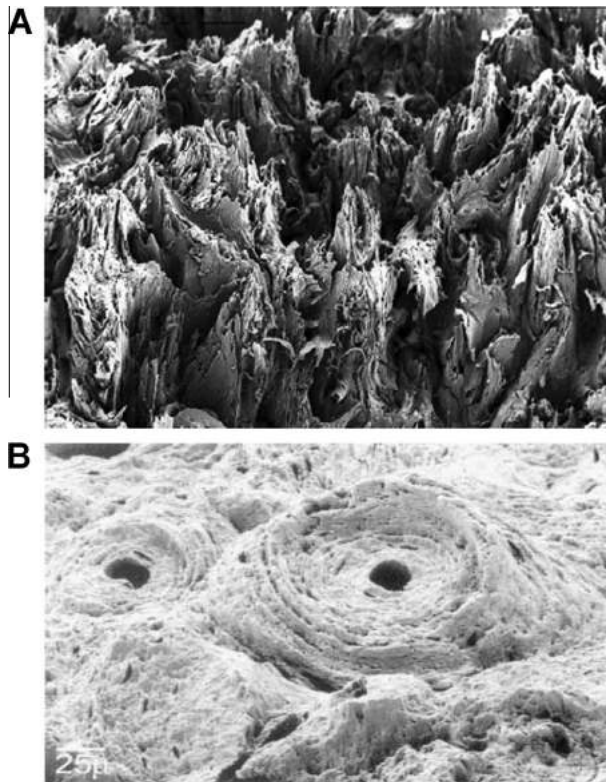


Fig. 13. (A) The fracture surface of a wet specimen from an elk (red deer) antler that was loaded to fracture in tension. The width of the picture is approximately 500 μm . The mineral content was about 48% of the wet weight. The work of fracture was about 6200 J m^{-2} . (Image and information are courtesy of J.D. Currey.) (B) Scanning electron micrograph of the transverse fracture surface of a cyclically loaded specimen from the dorsal cortex of a third metacarpal of an adult horse. Disruption of interlamellar and cement line interfaces reveals concentric lamellae and the outer osteon boundary of “pulled out” osteons. The width of the image is 293 μm . (Image reproduced from Hiller et al. (2003) with permission of R.B. Martin and John Wiley and Sons, Inc.).

Antler bone grows very quickly, yet apart from the fact that it is less well mineralized than most other bone, it does not have an unusual histology. The compact cortex contained a dense array of primary and secondary osteons. The formation of osteons appeared complete; there were very few erosion cavities or large primary vascular cavities. Polarized light microscopy of longitudinal and transverse sections suggests the mineralized fibres in the antler to be strongly preferentially arranged in the longitudinal direction.

By contrast, the results of the present study reveal much greater histological complexity. Additionally, dispersion of microcracks into the convoluted/hyper-mineralized interfacial seams (where CFO also tends to have increased oblique-to-transverse orienta-

tion) has been shown with two different imaging technologies. The first is scanning electron microscope images of fracture surfaces of the antler specimens showing osteonal/interfacial debonding, bridging, pullout, and “interlamellar” delaminations (e.g., “telescoping” patterns) (Chen et al., 2009; Launey et al., 2010b; Rajaram and Ramanathan, 1982; Zioupos et al., 1996) that appear to be extreme examples when compared to the osteon pullout and intra-osteonal interlamellar delaminations at fracture surfaces of secondary osteonal bone (Fig. 13) (Braidotti et al., 1997; Hiller et al., 2003; Liu et al., 2000). The second is real-time environmental SEM videography and post-test synchrotron X-ray micro-computed tomography (μXCT) of mechanically tested antler specimens (Launey et al., 2010b) (Fig. 1B; footnote 2). Although not definitively revealed by μXCT videography, there is also probable subsequent slippage along and/or in the vicinity of these hypermineralized seams/zones (Kulin et al., 2011). In view of these data, the primary osteonal bone of antler exhibits mechanical behavior that resembles fiber-reinforced ceramic matrix composite materials (Mohsin et al., 2006; Ritchie et al., 1993) – an analogy commonly drawn with the microstructural organization of secondary osteonal bone (Doblaré et al., 2004; Martin et al., 1998; Najafi et al., 2009; Nalla et al., 2005a,b; Yeni et al., 1997).

Our 3D data show osteon/vessel orientations that are consistent with rapid growth longitudinally and, though to a lesser extent, radially (Clark et al., 2006; de Margerie et al., 2004). We argue that the opinions stated in many prior studies of antler microstructure oversimplify osteon/vessel orientation as being along the long axis of the beam. This oversimplification steers discussions of toughening mechanisms in antler away from the potential importance of the non-longitudinal osteon orientations and, likely most importantly, the more irregular osteon interconnections. For example, when referring to microscopic images from fallow deer antlers (*Dama dama*) (Fig. 14), Rolf and Enderle (1999) state: “Osteons [sic.] consisting of concentric (Haversian) and interstitial lamellae are mainly orientated in the long axis of the antler shaft.” (pg. 70). Our scrutiny of the 2D images available in their study and the studies of others (e.g., Table 1), when considered in view of our findings, show that antler osteons/vascular canals are preferentially longitudinally oriented, but less pronounced than previously reported. The osteon canal orientations are at least as oblique as secondary osteons of long bone shafts habitually loaded in torsion, where oblique osteon orientations are thought to be adaptations for oblique principal strains and deleterious shear stresses engendered by torsional loading (Cooper et al., 2003; Martin and Burr, 1989; Petrářl et al., 1996).

We estimated that nearly 70% of the osteons in the 2D images published in three prior studies (Chen et al., 2009; Krauss et al., 2009; Launey et al., 2010b), and also in our 2D images, deviate by more than 45° with respect to the long axis of the antler beam (Table 1 and Fig. 15). Measurements of canal orientations made using our 3D micro-CT reconstructed images, however, show that



Fig. 14. Three microscopic images from antlers of adult fallow deer (*Dama dama*) from the study of Rolf and Enderle (1999). The arrows in B and C indicate the surface of the main beam. Note that there seems to be considerable vessel obliquity, which is especially notable in B and C. The approximate image widths are: (A) $300 \mu\text{m} \times 450 \mu\text{m}$ ($0.3 \text{ mm} \times 0.45 \text{ mm}$); (B) $4.8 \text{ mm} \times 7.2 \text{ mm}$; (C) $2.3 \text{ mm} \times 3.6 \text{ mm}$ (personal communication H.F. Rolf). (Images are courtesy of H.F. Rolf.)

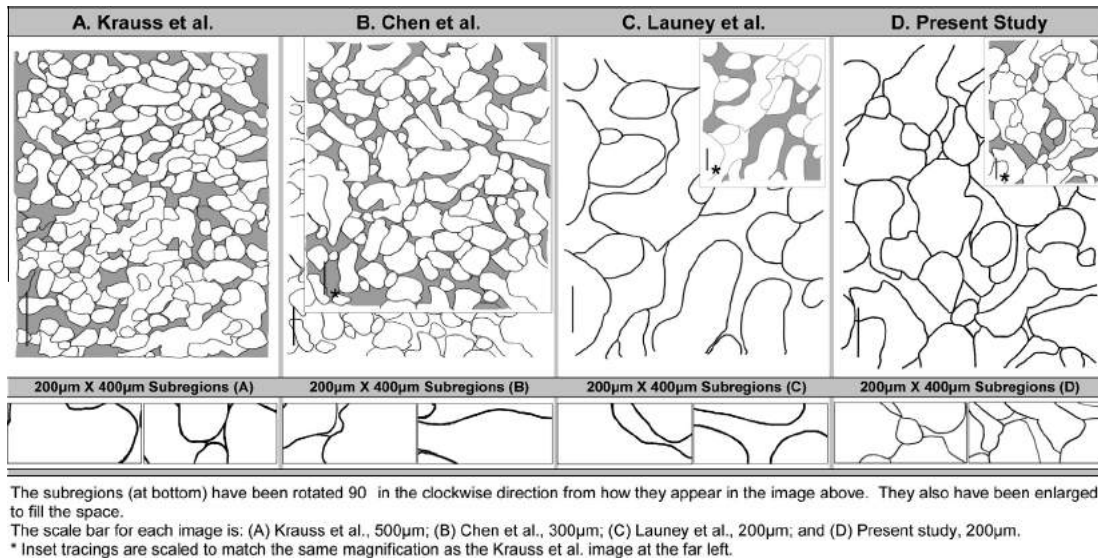


Fig. 15. Examples of interfaces drawn in $400\ \mu\text{m} \times 200\ \mu\text{m}$ areas (tracings at bottom) that were randomly selected from images published in: (A) Krauss et al. (2009), (B) Chen et al. (2009), and (C) Launey et al. (2010b), and from microscopic antler images from the present study (D). Notably, it is not possible to obtain a $400\ \mu\text{m} \times 200\ \mu\text{m}$ area in any of these images without including interfaces. The grayed areas in the traced images indicate regions that were not used for quantification of parameters from individual osteons (either because the osteons are difficult to trace and/or represent bone of the trabecular scaffold). Also, the osteons traversing across the border of the image were not used for the osteon circularity or elongation analyses shown in Tables 1 and 2.

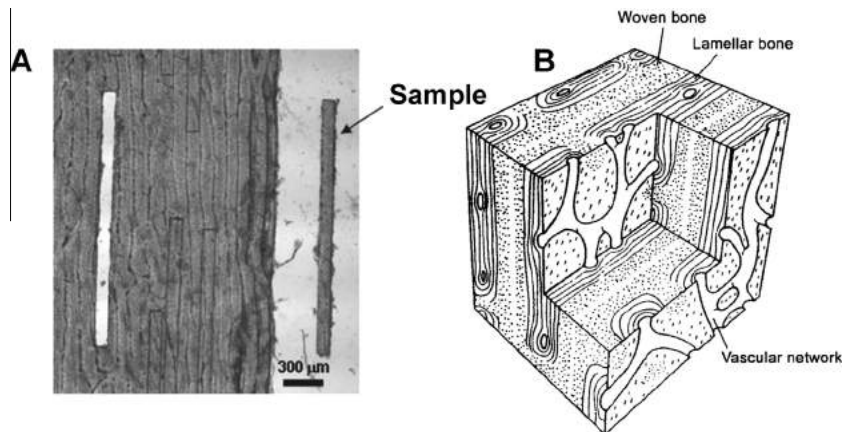


Fig. 16. (A) Image of bovine primary bone with one lamellar “sheet” (at right is the “sample”) from Gupta et al. (2006a), which is from the plexiform-vascularization type of fibrolamellar bone. (Images reprinted with permission of the authors and Elsevier Inc.); (B) Drawing of fibrolamellar bone adapted from Currey (see Skedros and Hunt, 2004).

these estimates are overstated. The 3D data show that approximately 65% of the vascular canals are actually within 20° of the long axis of the antler beam (Fig. 12A) (41% of canals are within 10° of the long axis, 55% are within 15° of the long axis, and 78% of the vascular canals are within 30° of the long axis). This clear discrepancy with our 2D estimations can be explained by: (1) our assumption that osteons are cylindrical, which is overly simplified for antler when compared to typical secondary osteons, and (2) there appears to be a much less-than-perfect correspondence between vascular canal orientation and osteon orientation (Figs. 7 and 8). Nevertheless, the fact that only approximately 55% of the antler osteonal structures are within 15° of the long axis of the antler beam distinguishes the microstructure of antler from that of typical long bones of the appendicular skeleton – where in limb long bones a much higher percentage (estimated at $>80\%$) of secondary osteons have been reported as being aligned within 15° of the longitudinal axis (Heřt et al., 1994; Martin and Burr, 1989).

Technical constraints inherent in the analysis of very small specimens pose challenges for discerning the relative importance of nanostructural vs. microstructural toughening mechanisms in

antler and other naturally occurring mineralized composite materials. These issues are illustrated by the specimen sizes and results of microanalytical analyses that have been used to contrast the mechanical behaviors of antler with data from bovine bone specimens that were reported in a previous series of elegant studies by Gupta and colleagues (Benecke et al., 2009; Gupta et al., 2006a, 2005). These three prior studies examined bovine fibrolamellar bone (Fig. 16), with only one bone typically being used in each study (unclear in Benecke et al.). The type of fibrolamellar bone that they examined appears to be most consistent with plexiform vascularization, but with relatively fewer radial vessels when compared to longitudinal and circular vessels (Fig. 16B). (Additional description of the differences between the histology of antler and bovine bone can be found in Appendix 2.) In these earlier studies of bovine fibrolamellar bone, Gupta and co-workers showed that the stress–strain curve started to plateau at the yield point with lower hierarchical levels of tissue organization (Fig. 17).

In other studies using the same experimental apparatus, Gupta and co-workers (Benecke et al., 2009; Gupta et al., 2005) used bovine fibrolamellar bone specimens that had the same

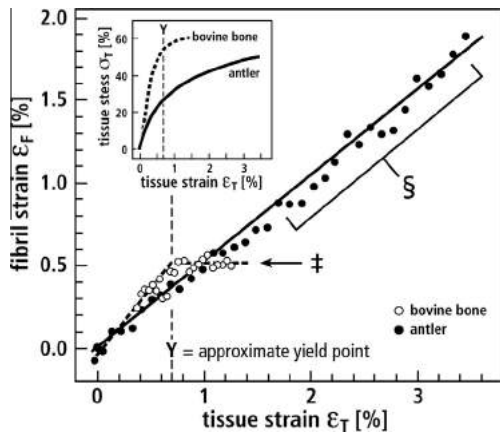


Fig. 17. Fibrillar vs. tissue strain curves from Krauss et al. (2009) and Gupta et al. (2006a). It is notable that the bovine specimens show a change in slope after yielding (“‡”). While this does not occur in the antler samples, the scatter does progressively increase with loading (“§”). We suggest that this increased scatter in antler hints at influences of microstructural/osteonal interfaces that are present within the specimen. We also speculate that the marked change in slope that occurs in the bovine specimens reflects the relatively more dramatic influence of the few radial canals that were retained in these specimens and were orthogonal to the direction of loading (hence likely having more substantial influence than the more circuitous/incomplete residual interfaces in antler). (Modified from the original version which was reprinted with permission of the authors and Elsevier Inc.)

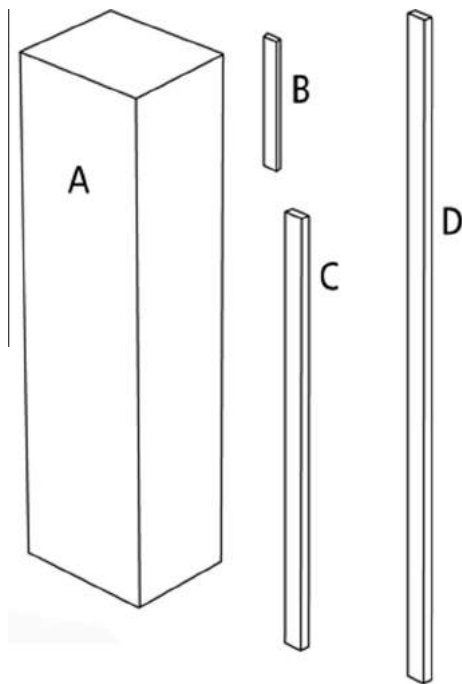


Fig. 18. Relative differences in the specimen sizes used in various studies: (A) elk antler from Launey et al. (2010b) (12 mm × 3 mm × 2.0–2.2 mm), (B) bovine fibrolamellar bone from Gupta et al. (2006a) (3 mm × 150 μm × 50 μm), (C) bovine fibrolamellar bone from Benecke et al. (2009) (10 mm × 400 μm × 200 μm), and (D) elk (red deer) antler from Krauss et al. (2009) and Gupta et al. (2013) and bovine fibrolamellar bone from Gupta et al. (2005) (16 mm × 400 μm × 200 μm).

cross-sectional dimensions as in their subsequent studies of antler (400 μm × 200 μm) (Gupta et al., 2013; Krauss et al., 2009) (Fig. 18). This 400 μm × 200 μm cross-sectional area could include up to approximately 3–4 “interfaces” of the fibrolamellar bone (and probably included some radial vessels). Importantly, and also

surprisingly, the results of Gupta et al. (2006a), which used single-sheet bovine specimens (3 mm × 150 μm × 50 μm), showed a change in the slope of the stress–strain curve at the yield point that was similar to the mechanical behavior of the larger matchstick-like (10 mm, or 16 mm, × 400 μm × 200 μm) bovine specimens that included more than one “sheet” (Benecke et al., 2009; Gupta et al., 2005).

In contrast to these studies of plexiform-vascularization fibrolamellar bone, their mechanical testing studies of antler showed that strains in antler did not gradually plateau with lower hierarchical levels (Gupta et al., 2013; Krauss et al., 2009) (e.g., “‡” vs. “§” in Fig. 17). Consequently, they concluded that although both antler and bovine fibrolamellar bone show similar nanoscale fibril shearing mechanisms during elastic deformation (i.e., pre-yield), they are different during inelastic deformation (i.e., after macroscopic yielding). They concluded that inhomogeneous fibril stretching occurs in antler leading to defects and consequent debonding between neighboring fibrils, and this mechanism predominates during post-yield loading. Consequently, they minimize an important role for the heterogeneous/complex microstructure that we report herein and also, by contrast, have been shown to be fundamentally important loci of extrinsic-level toughening before (Kulin et al., 2011; Launey et al., 2010b) and after (Kulin et al., 2011) macroscopic yielding of North American elk antler.

But, at this time, it is difficult to accept this conclusion, and the implication that this is the dominant physical basis of the extraordinary toughness of antler. One reason is that only one antler was used in each of these studies. The other reason is that the matchstick-like specimen sizes used in the series of experiments by Krauss et al. (2009) and Gupta et al. (2013) may effectively eliminate the physiologic effects that microstructural characteristics might have on extrinsic microcracking during bulk testing (Hoo et al., 2011; Kulin et al., 2011). The study of Kulin et al. (2011) is also, and perhaps even more severely limited because: (1) only one antler was used and was collected one year after being shed, (2) the antler was obtained from a commercial store where the storage conditions were likely less than ideal, and (3) it was tested at high strain rates using an unusual methodology. They used the Split-Hopkinson Pressure Bar layout for their mechanical testing, which has been shown to have limitations for testing low strain-to-failure materials because premature failure occurs prior to the attainment of equilibrium conditions in the specimen (Sunny et al., 2009). They attempted to minimize this by using a ‘pulse shaper’ to cushion the impact. However, given this method’s overall inherent limitations, their results are challenging to compare with results of the other authors who use standard methods conducted at much slower strain rates. While the methodology allows for the testing of true impact loading scenarios, further testing of more (and fresher) samples are needed to validate the method and confirm the results of Kulin et al. (2011).

An additional challenge is to develop methodologies that allow quantification of extrinsic vs. intrinsic failure mechanisms in bulk specimens. The influences of microstructural interfaces and the composition and ultrastructural organization of the adjacent vs. more distant matrix on the mechanical behavior of the tissue would require testing larger specimens as has been revealed in studies of relatively larger specimens of North American elk antler (Launey et al., 2010b) and in bovine fibrolamellar (Hoo et al., 2011) and secondary-osteonal human (Zimmermann et al., 2011) cortical bone. For example, Hoo et al. (2011) show how starkly contradictory conclusions can be when testing bone tissue with different length scales, specimen volumes, and microstructures. In fact, they report data from bulk specimens that refute the findings of Gupta et al. (2006a,b, 2005) that emphasized the importance of fibrillar-level failure in bovine fibrolamellar bone beyond the yield point.

5. Conclusion

It is probable that extrinsic/microscale collagen-based characteristics (e.g., localized CFO heterogeneity) and hypermineralized seams/"zones", in addition to their spatial associations with complex morphology of the osteonal interfaces described herein contribute significantly in conferring the extraordinary toughness of antler. These microstructural characteristics are more extreme/dramatic than what has been shown in secondary osteonal bone where they are considered adaptations that extrinsically toughen the bone for habitual tension and shear strain environments. However, the issue at hand is the extent to which both intrinsic and extrinsic mechanisms contribute to the extraordinary toughness of antler. Certainly unusual/unique interactions of nanoscale and microscale failure mechanisms are likely at work in elastic/inelastic transition in antler. But we believe that details about how this works have yet to be fully resolved in robust sample sizes that are subjected to experiments that mirror natural loading conditions.

Acknowledgments

The authors would like to acknowledge Tyler R. Epperson for his assistance with BSE imaging.

Appendix 1. Intrinsic vs. extrinsic toughening: considerations at the nanoscale and microscale

Gupta et al. (2006a,b) and Launey et al. (2010a) list several potentially important toughening mechanisms in bone, including antler, that are either "intrinsic" (ahead of a crack tip and <1 μm in scale) or "extrinsic" (behind a crack tip and >1 μm in scale). The *intrinsic* mechanisms include: (1) molecular uncoiling (Gautieri et al., 2011), (2) shear transfer between mineral particles via intermediate ductile organic layers (Jäger and Fratzl, 2000), (3) slippage at the collagen-mineral interface (Mercer et al., 2006), (4) phase transformation of the mineral phase (Carden et al., 2003), (5) sacrificial bond disruption between fibrils (Fantner et al., 2005), and (6) microcracking (Ziopoulos, 1999) which typically precedes the larger scale "extrinsic" microcracking that often involves osteons. The *extrinsic* mechanisms include: (1) constrained microcracking, and (2) microcrack deflection and twist, and microcrack bridging (Launey et al., 2010b; Nalla et al., 2003). The importance of microcracking extrinsically is that it results in both microcrack bridging and deflection, which are the most potent toughening mechanisms in bone and have been shown to typically involve osteonal structures and/or other microstructural interfaces (Hoo et al., 2011; Launey et al., 2010a; Ritchie et al., 2005).

Other possible extrinsic toughening mechanisms in antler and other bones that are more highly mineralized include variations in CFO, including regionally increased oblique-to-transverse CFO near osteonal interfaces and around the vascular canal lumens (as found in the present study) and/or other possible characteristics of collagen organization and composition not studied herein (e.g., spatial variations in the collagen molecular cross-links and regional variations in types and concentrations of non-collagenous proteins) (Ingram et al., 1993; Saito and Marumo, 2010; Skedros et al., 2009, 2011). Several studies of mammalian limb bones suggest that these variations can contribute in toughening (Burstein et al., 1975; Fratzl-Zelman et al., 2009; Hiller et al., 2003; Shelton et al., 2000; Wang et al., 2001, 2002; Ziopoulos et al., 1999). There is evidence that some of the above mentioned collagen-based characteristics are also mechanically important in ways that are independent of the areal/volumetric density and morphology of osteonal interfaces. For example, in human bone, Wang et al.

(2001) showed that the percentage of denatured collagen compared to the total collagen content is significantly related to failure energy and fracture toughness, supporting the idea that collagen in bone is a primary arrestor of microcracks (Burr, 2002; Sobelman et al., 2004). In their study of failure testing of bulk antler specimens in compression, Kulin et al. (2011) concluded that the collagen component accounts in large part for the compressive strains observed in antler in excess of 20%. In these perspectives it is probable that CFO heterogeneity described in the present study and possibly other aforementioned collagen-based characteristics that were not studied (e.g., collagen molecular cross-links) contribute significantly in conferring the extraordinary toughness of antler in addition to the influences of this tissue's hypermineralized seams/zones, complex morphology of the osteonal interfaces, and relatively reduced overall mineral content.

Appendix 2. Histology of antler vs. bovine fibrolamellar bone

The primary osteonal structure of antler contrasts with the histomorphology of primary bovine bone — the latter is often called fibrolamellar bone (also known, but less precisely, as laminar or plexiform bone) (Mori et al., 2003; Paral et al., 2007). In fibrolamellar bone, primary osteonal structures such as those seen in antler are either entirely absent or are comparatively less prevalent (Currey, 2002; Mori et al., 2003). In fibrolamellar bone there are laminae that are approximately 200 μm thick, and in the middle of a lamina is a network of blood vessels that is sheathed by lamellar bone; these regions alternate with layers of woven bone (Fig. 16). Different types of fibrolamellar bone are distinguished by their patterns of lamellar-sheathed vascular architecture, which span the spectrum from the simpler two-dimensional to more complex three-dimensional vessel arrangements: (1) laminar vascularization = longitudinal and circular vascular canals, (2) plexiform vascularization = radial, longitudinal, and circular vascular canals, and (3) reticular vascularization = oblique vascular canals (de Ricqlès et al., 1991; Skedros and Hunt, 2004). In a study of relationships between bone growth rates and histological patterns/differences in limbs of king penguins, de Margerie et al. (2004) considered four types of fibrolamellar bone: (1) laminar (i.e., high percentage of circular canals in addition to longitudinally oriented canals), (2) longitudinal, (3) reticular, and (4) radial.

Appendix B. Supplementary data

Supplementary data associated with this article can be found, in the online version, at <http://dx.doi.org/10.1016/j.jsb.2014.06.004>.

References

- Banks, W.J., Glenwood, P.E., Kainer, R.A., 1968. Antler growth and osteoporosis: morphological and morphometric changes in the costal compacta during the antler growth cycle. *Anat. Rec.* 162, 387–398.
- Barth, H.D., Launey, M.E., Macdowell, A.A., Ager 3rd, J.W., Ritchie, R.O., 2010. On the effect of X-ray irradiation on the deformation and fracture behavior of human cortical bone. *Bone* 46, 1475–1485.
- Benecke, G., Kerschitzki, M., Fratzl, P., Gupta, H.S., 2009. Digital image correlation shows localized deformation bands in inelastic loading of fibrolamellar bone. *J. Mater. Res.* 24, 421–429.
- Beraudi, A., Stea, S., Bordini, B., Baleani, M., Viceconti, M., 2010. Osteon classification in human fibular shaft by circularly polarized light. *Cells Tissues Organs* 191, 260–268.
- Bigley, R.F., Griffin, L.V., Christensen, L., Vandenbosch, R., 2006. Osteonal interfacial strength and histomorphometry of equine cortical bone. *J. Biomech.* 39, 1629–1640.
- Blob, R.W., Snelgrove, J.M., 2006. Antler stiffness in moose (*Alces alces*): correlated evolution of bone function and material properties? *J. Morphol.* 267, 1075–1086.
- Bloebaum, R.D., Holmes, J.L., Skedros, J.G., 2005. Mineral content changes in bone associated with damage induced by the electron beam. *Scanning* 27, 240–248.

- Bloebaum, R.D., Lundeen, G.A., Shea, J.E., Whitaker, E.L., 2004. Age-related mineralization heterogeneity changes in trabecular bone of the proximal femur. *Anat. Rec. A Discov. Mol. Cell. Evol. Biol.* 281, 1296–1302.
- Bloebaum, R.D., Skedros, J.G., Vajda, E.G., Bachus, K.N., Constantz, B.R., 1997. Determining mineral content variations in bone using backscattered electron imaging. *Bone* 20, 485–490.
- Boskey, A.L., 2001. Bone mineralization. In: Cowin, S.C. (Ed.), *Bone Mechanics Handbook*. CRC Press, Boca Raton (p. 5–1–5–33).
- Boyce, T.M., Bloebaum, R.D., Bachus, K.N., Skedros, J.G., 1990. Reproducible methods for calibrating the backscattered electron signal for quantitative assessment of mineral content in bone. *Scanning Microsc.* 4, 591–600 (discussion 600–593).
- Boyde, A., Riggs, C.M., 1990. The quantitative study of the orientation of collagen in compact bone slices. *Bone* 11, 35–39.
- Braidotti, P., Branca, F.P., Stagni, L., 1997. Scanning electron microscopy of human cortical bone failure surfaces. *J. Biomech.* 30, 155–162.
- Britz, H.M., Jokihara, J., Leppanen, O.V., Jarvinen, T.L., Cooper, D.M., 2012. The effects of immobilization on vascular canal orientation in rat cortical bone. *J. Anat.* 220, 67–76.
- Bromage, T.G., Goldman, H.M., McFarlin, S.C., Warshaw, J., Boyde, A., et al., 2003. Circularly polarized light standards for investigations of collagen fiber orientation in bone. *Anat. Rec.* 274B, 157–168.
- Burr, D.B., 2002. The contribution of the organic matrix to bone's material properties. *Bone* 31, 8–11.
- Burstein, A.H., Zika, J.M., Heiple, K.G., Klein, L., 1975. Contribution of collagen and mineral to the elastic-plastic properties of bone. *J. Bone Joint Surg. Am.* 57, 956–961.
- Carden, A., Rajachar, R.M., Morris, M.D., Kohn, D.H., 2003. Ultrastructural changes accompanying the mechanical deformation of bone tissue: a Raman imaging study. *Calcif. Tissue Int.* 72, 166–175.
- Chapman, D., 1975. Antlers-bones of contention. *Mammal Rev.* 5, 121–172.
- Chen, P.Y., Stokes, A.G., McKittrick, J., 2009. Comparison of the structure and mechanical properties of bovine femur bone and antler of the North American elk (*Cervus elaphus canadensis*). *Acta Biomater.* 5, 693–706.
- Ciarelli, T.E., Tjhia, C., Rao, D.S., Qiu, S., Parfitt, A.M., et al., 2009. Trabecular packet-level lamellar density patterns differ by fracture status and bone formation rate in white females. *Bone* 45, 903–908.
- Clark, D.E., Li, C., Wang, W., Martin, S.K., Suttie, J.M., 2006. Vascular localization and proliferation in the growing tip of the deer antler. *Anat. Rec. A Discov. Mol. Cell. Evol. Biol.* 288, 973–981.
- Clutton-Brock, T.H., 1982. The functions of antlers. *Behaviour* 79, 108–125.
- Cooper, D.M., Turinsky, A.L., Sensen, C.W., Hallgrímsson, B., 2003. Quantitative 3D analysis of the canal network in cortical bone by micro-computed tomography. *Anat. Rec. B New Anat.* 274, 169–179.
- Currey, J.D., 1979. Mechanical properties of bone tissues with greatly differing functions. *J. Biomech.* 12, 313–319.
- Currey, J.D., 1984. Effects of differences in mineralization on the mechanical properties of bone. *Philos. Trans. R. Soc. Lond. B Biol. Sci.* 304, 509–518.
- Currey, J.D., 1990. Physical characteristics affecting the tensile failure properties of compact bone. *J. Biomech.* 23, 837–844.
- Currey, J.D., 2002. *Bones: Structure and Mechanics*. Princeton University Press, Princeton, NJ.
- Currey, J.D., Landete-Castillejos, T., Estevez, J., Ceacero, F., Olguin, A., et al., 2009. The mechanical properties of red deer antler bone when used in fighting. *J. Exp. Biol.* 212, 3985–3993.
- de Margerie, E., Robin, J.P., Verrier, D., Cubo, J., Groscolas, R., et al., 2004. Assessing a relationship between bone microstructure and growth rate: a fluorescent labelling study in the king penguin chick (*Aptenodytes patagonicus*). *J. Exp. Biol.* 207, 869–879.
- de Ricolès, A., Meunier, F.J., Castanet, L., Francillon-Vieillot, H., 1991. Comparative microstructure of bone. In: Hall, B.K. (Ed.), *Bone*. CRC Press, Boca Raton, FL, pp. 1–78.
- Doblaré, M., García Aznar, J.M., Gómez, M.J., 2004. Modelling bone tissue fracture and healing: a review. *Eng. Fract. Mech.* 71, 1809–1840.
- Donahue, S.W., Galley, S.A., 2006. Microdamage in bone: implications for fracture, repair, remodeling, and adaptation. *Crit. Rev. Biomed. Eng.* 34, 215–271.
- Dong, X.N., Almer, J.D., Wang, X., 2011. Post-yield nanomechanics of human cortical bone in compression using synchrotron X-ray scattering techniques. *J. Biomech.* 44, 676–682.
- Ebacher, V., Tang, C., McKay, H., Oxland, T.R., Guy, P., et al., 2007. Strain redistribution and cracking behavior of human bone during bending. *Bone* 40, 1265–1275.
- Emmanuel, J., Hornbeck, C., Bloebaum, R.D., 1987. A polymethyl methacrylate method for large specimens of mineralized bone with implants. *Stain Technol.* 62, 401–410.
- Fantner, G.E., Hassenkam, T., Kindt, J.H., Weaver, J.C., Birkedal, H., et al., 2005. Sacrificial bonds and hidden length dissipate energy as mineralized fibrils separate during bone fracture. *Nat. Mater.* 4, 612–616.
- Fratzl-Zelman, N., Roschger, P., Gourrier, A., Weber, M., Misof, B.M., et al., 2009. Combination of nanoindentation and quantitative backscattered electron imaging revealed altered bone material properties associated with femoral neck fragility. *Calcif. Tissue Int.* 85, 335–343.
- Gautieri, A., Vesentini, S., Redaelli, A., Buehler, M.J., 2011. Hierarchical structure and nanomechanics of collagen microfibrils from the atomistic scale up. *Nano Lett.* 11, 757–766.
- Gomez, S., Garcia, A.J., Luna, S., Kierdorf, U., Kierdorf, H., et al., 2013. Labeling studies on cortical bone formation in the antlers of red deer (*Cervus elaphus*). *Bone* 52, 506–515.
- Gupta, H.S., Seto, J., Wagermaier, W., Zaslansky, P., Boesecke, P., et al., 2006a. Cooperative deformation of mineral and collagen in bone at the nanoscale. *Proc. Natl. Acad. Sci. USA* 103, 17741–17746.
- Gupta, H.S., Wagermaier, W., Zickler, G.A., Raz-Ben Aroush, D., Funari, S.S., et al., 2005. Nanoscale deformation mechanisms in bone. *Nano Lett.* 5, 2108–2111.
- Gupta, H.S., Wagermaier, W., Zickler, G.A., Hartmann, J., Funari, S.S., et al., 2006b. Fibrillar level fracture in bone beyond the yield point. *Int. J. Fract.* 139, 425–436.
- Gupta, H.S., Krauss, S., Kerschitzki, M., Karunaratne, A., Dunlop, J.W., et al., 2013. Intrafibrillar plasticity through mineral/collagen sliding is the dominant mechanism for the extreme toughness of antler bone. *J. Mech. Behav. Biomed. Mater.* 28, 366–382.
- Harrigan, T.P., Mann, R.W., 1984. Characterization of microstructural anisotropy in orthotropic materials using a second rank tensor. *J. Mater. Sci.* 19, 761–767.
- Heft, J., Fiala, P., Petrtyl, M., 1994. Osteon orientation of the diaphysis of the long bones in man. *Bone* 15, 269–277.
- Hiller, L.P., Stover, S.M., Gibson, V.A., Gibeling, J.C., Prater, C.S., et al., 2003. Osteon pullout in the equine third metacarpal bone: Effects of *ex vivo* fatigue. *J. Orthop. Res.* 21, 481–488.
- Hintze, J., 1995. *Number Cruncher Statistical Systems 6.0 User's Manual*. Kaysville, Utah.
- Hirth, D.H., 1977. Social behavior of white-tailed deer in relation to habitat. *Wildlife Monographs* 53, 1–55.
- Holmes, J.L., Bachus, K.N., Bloebaum, R.D., 2000. Thermal effects of the electron beam and implications of surface damage in the analysis of bone tissue. *Scanning* 22, 243–248.
- Hoo, R.P., Fratzi, P., Daniels, J.E., Dunlop, J.W., Honkima, V., et al., 2011. Cooperation of length scales and orientations in the deformation of bovine bone. *Acta Biomater.* 7, 2943–2951.
- Ingram, R.T., Clarke, B.L., Fisher, L.W., Fitzpatrick, L.A., 1993. Distribution of noncollagenous proteins in the matrix of adult human bone: evidence of anatomic and functional heterogeneity. *J. Bone Miner. Res.* 8, 1019–1029.
- Jager, I., Fratzi, P., 2000. Mineralized collagen fibrils: a mechanical model with a staggered arrangement of mineral particles. *Biophys. J.* 79, 1737–1746.
- Kierdorf, U., Kierdorf, H., Boyde, A., 2000. Structure and mineralisation density of antler and pedicle bone in red deer (*Cervus elaphus* L.) exposed to different levels of environmental fluoride: a quantitative backscattered electron imaging study. *J. Anat.* 196 (Pt 1), 71–83.
- Kierdorf, U., Flohr, S., Gomez, S., Landete-Castillejos, T., Kierdorf, H., 2013. The structure of pedicle and hard antler bone in the European roe deer (*Capreolus capreolus*): a light microscope and backscattered electron imaging study. *J. Anat.* 223, 364–384.
- Koester, K.J., Ager 3rd, J.W., Ritchie, R.O., 2008. The true toughness of human cortical bone measured with realistically short cracks. *Nat. Mater.* 7, 672–677.
- Krauss, S., Wagermaier, W., Estevez, J.A., Currey, J.D., Fratzi, P., 2011. Tubular frameworks guiding orderly bone formation in the antler of the red deer (*Cervus elaphus*). *J. Struct. Biol.* 175, 457–464.
- Krauss, S., Fratzi, P., Seto, J., Currey, J.D., Estevez, J.A., et al., 2009. Inhomogeneous fibril stretching in antler starts after macroscopic yielding: indication for a nanoscale toughening mechanism. *Bone* 44, 1105–1110.
- Kulin, R.M., Chen, P., Jiang, F., Vecchio, K.S., 2011. A study of the dynamic compressive behavior of elk antler. *Mater. Sci. Eng. C* 31, 1030–1041.
- Landete-Castillejos, T., Garcia, A., Gallego, L., 2007a. Body weight, early growth and antler size influence antler bone mineral composition of Iberian red deer (*Cervus elaphus hispanicus*). *Bone* 40, 230–235.
- Landete-Castillejos, T., Currey, J.D., Estevez, J.A., Gaspar-Lopez, E., Garcia, A., et al., 2007b. Influence of physiological effort of growth and chemical composition on antler bone mechanical properties. *Bone* 41, 794–803.
- Landete-Castillejos, T., Currey, J.D., Ceacero, F., Garcia, A.J., Gallego, L., et al., 2012. Does nutrition affect bone porosity and mineral tissue distribution in deer antlers? The relationship between histology, mechanical properties and mineral composition. *Bone* 50, 245–254.
- Landete-Castillejos, T., Currey, J.D., Estevez, J.A., Fierro, Y., Calatayud, A., et al., 2010. Do drastic weather effects on diet influence changes in chemical composition, mechanical properties and structure in deer antlers? *Bone* 47, 815–825.
- Launey, M.E., Buehler, M.J., Ritchie, R.O., 2010a. On the mechanistic origins of toughness in bone. *Annu. Rev. Mater. Res.* 40, 25–53.
- Launey, M.E., Chen, P.Y., McKittrick, J., Ritchie, R.O., 2010b. Mechanistic aspects of the fracture toughness of elk antler bone. *Acta Biomater.* 6, 1505–1514.
- Leng, H., Dong, X.N., Wang, X., 2009. Progressive post-yield behavior of human cortical bone in compression for middle-aged and elderly groups. *J. Biomech.* 42, 491–497.
- Liu, D., Wagner, H.D., Weiner, S., 2000. Bending and fracture of compact circumferential and osteonal lamellar bone of the baboon tibia. *J. Mater. Sci. Mater. Med.* 11, 49–60.
- Martin, R.B., Burr, D.B., 1989. *Structure, Function and Adaptation of Compact Bone*. Raven Press, New York.
- Martin, R.B., Burr, D.B., Sharkey, N.A., 1998. *Skeletal Tissue Mechanics*. Springer-Verlag, New York, NY.
- McKee, M.D., Nanci, A., 1996. Osteopontin at mineralized tissue interfaces in bone, teeth, and osseointegrated implants: ultrastructural distribution and implications for mineralized tissue formation, turnover, and repair. *Microsc. Res. Tech.* 33, 141–164.

- Mercer, C., He, M.Y., Wang, R., Evans, A.G., 2006. Mechanisms governing the inelastic deformation of cortical bone and application to trabecular bone. *Acta Biomater.* 2, 59–68.
- Mohsin, S., O'Brien, F.J., Lee, T.C., 2006. Osteonal crack barriers in ovine compact bone. *J. Anat.* 208, 81–89.
- Mori, R., Kodaka, T., Sano, T., Yamagishi, N., Asari, M., et al., 2003. Comparative histology of the laminar bone between young calves and foals. *Cells Tissues Organs* 175, 43–50.
- Najafi, A., Arshi, A., Saffar, K., Eslami, M., Fariborz, S., et al., 2009. A fiber-ceramic matrix composite material model for osteonal cortical bone fracture micromechanics: solutions of arbitrary microcracks interaction. *J. Mech. Behav. Biomed.* 2, 217–223.
- Nalla, R.K., Kinney, J.H., Ritchie, R.O., 2003. Mechanistic fracture criteria for the failure of human cortical bone. *Nat. Mater.* 2, 164–168.
- Nalla, R.K., Kruzic, J.J., Kinney, J.H., Ritchie, R.O., 2005a. Mechanistic aspects of fracture and R-curve behavior in human cortical bone. *Biomaterials* 26, 217–231.
- Nalla, R.K., Stolken, J.S., Kinney, J.H., Ritchie, R.O., 2005b. Fracture in human cortical bone: local fracture criteria and toughening mechanisms. *J. Biomech.* 38, 1517–1525.
- Neville, A.C., 1980. Optical methods in cuticle research. In: Miller, T.A. (Ed.), *Cuticle Techniques in Arthropods*. Springer-Verlag, New York, NY, pp. 45–89.
- Norman, T.L., Wang, Z., 1997. Microdamage of human cortical bone: Incidence and morphology in long bones. *Bone* 20, 375–379.
- Nowak, R.M., 1999. *Walker's Mammals of the World*, sixth ed. The John Hopkins University Press, New York.
- O'Brien, F., Taylor, D., Lee, T.C., 2005a. The effect of bone microstructure on the initiation and growth of microcracks. *J. Orthop. Res.* 23, 475–480.
- O'Brien, F., Taylor, D., Lee, T., 2007. Bone as a composite material: the role of osteons as barriers to crack growth in compact bone. *Int. J. Fatigue* 29, 1051–1056.
- O'Brien, F., Hardiman, D.A., Hazenberg, J.G., Mercy, M.V., Mohsin, S., et al., 2005b. The behaviour of microcracks in compact bone. *Eur. J. Morphol.* 42, 71–79.
- Olvera, D., Zimmermann, E.A., Ritchie, R.O., 2012. Mixed-mode toughness of human cortical bone containing a longitudinal crack in far-field compression. *Bone* 50, 331–336.
- Paral, V., Witter, K., Tonar, Z., 2007. Microscopic examination of ground sections – a simple method for distinguishing between bone and antler? *Int. J. Osteoarchaeology* 17, 627–634.
- Peterlik, H., Roschger, P., Klaushofer, K., Fratzl, P., 2006. From brittle to ductile fracture of bone. *Nat. Mater.* 5, 52–55.
- Petrtyl, M., Hert, J., Fiala, P., 1996. Spatial organization of Haversian bone in man. *J. Biomech.* 29, 161–169.
- Rajaram, A., Ramanathan, N., 1982. Tensile properties of antler bone. *Calcif. Tissue Int.* 34, 301–305.
- Rasband, W., 1997–2009. *ImageJ*, 1.43 ed. U.S. National Institutes of Health, Bethesda, Maryland.
- Ritchie, R.O., Kinney, J.H., Kruzic, J.J., Nalla, R.K., 2005. A fracture mechanics and mechanistic approach to the failure of cortical bone. *Fatigue Fract. Eng. Mater. Struct.* 28, 345–371.
- Ritchie, R.O., Cannon, R.M., Dalgleish, B.J., Dauskardt, R.H., McNaney, J.M., 1993. Mechanics and mechanisms of crack growth at or near ceramic-metal interfaces: interface engineering strategies for promoting toughness. *Mater. Sci. Eng. A* 166, 221–235.
- Rolf, H.J., Enderle, A., 1999. Hard fallow deer antler: a living bone till antler casting? *Anat. Rec.* 255, 69–77.
- Ruffoni, D., Fratzl, P., Roschger, P., Klaushofer, K., Weinkamer, R., 2007. The bone mineralization density distribution as a fingerprint of the mineralization process. *Bone* 40, 1308–1319.
- Saito, M., Marumo, K., 2010. Collagen cross-links as a determinant of bone quality: a possible explanation for bone fragility in aging, osteoporosis, and diabetes mellitus. *Osteoporos. Int.* 21, 195–214.
- Shelton, D.R., Gibeling, J.C., Martin, R.B., Stover, S.M., 2000. Fatigue crack growth rates in equine cortical bone. *Trans. Am. Soc. Biomech.* 24, 247–248.
- Skedros, J., Hughes, P., Nelson, K., Winet, H., 1999. Collagen Fiber Orientation in the Proximal Femur: Challenging Wolff's Tension/Compression Interpretation. *Journal of Bone and Mineral Research: Twenty-First Annual Meeting of the American Society for Bone and Mineral Research*, St. Louis, Missouri.
- Skedros, J.G., 1995. Hypermineralized peripheral lamellae in primary osteons of deer antler: potential functional analogues of cement lines in mammalian secondary bone. *J. Bone Miner. Res.* 10, S441.
- Skedros, J.G., 2012. Interpreting load history in limb-bone diaphyses: important considerations and their biomechanical foundations. In: Crowder, C., Stout, S. (Eds.), *Bone Histology: An Anthropological Perspective*. CRC Press, Boca Raton, Florida, pp. 153–220.
- Skedros, J.G., Hunt, K.J., 2004. Does the degree of laminarity mediate site-specific differences in collagen fiber orientation in primary bone? An evaluation in the turkey ulna diaphysis. *J. Anat.* 205, 121–134.
- Skedros, J.G., Su, S.C., Bloebaum, R.D., 1997. Biomechanical implications of mineral content and microstructural variations in cortical bone of horse, elk, and sheep calcanei. *Anat. Rec.* 249, 297–316.
- Skedros, J.G., Mason, M.W., Bloebaum, R.D., 2001. Modeling and remodeling in a developing artiodactyl calcaneus: a model for evaluating Frost's mechanostat hypothesis and its corollaries. *Anat. Rec.* 263, 167–185.
- Skedros, J.G., Bloebaum, R.D., Bachus, K.N., Boyce, T.M., 1993a. The meaning of graylevels in backscattered electron images of bone. *J. Biomed. Mater. Res.* 27, 47–56.
- Skedros, J.G., Mason, M.W., Nelson, M.C., Bloebaum, R.D., 1996. Evidence of structural and material adaptation to specific strain features in cortical bone. *Anat. Rec.* 246, 47–63.
- Skedros, J.G., Holmes, J.L., Vajda, E.G., Bloebaum, R.D., 2005. Cement lines of secondary osteons in human bone are not mineral-deficient: new data in a historical perspective. *Anat. Rec. A Discov. Mol. Cell. Evol. Biol.* 286, 781–803.
- Skedros, J.G., Mendenhall, S.D., Kiser, C.J., Winet, H., 2009. Interpreting cortical bone adaptation and load history by quantifying osteon morphotypes in circularly polarized light images. *Bone* 44, 392–403.
- Skedros, J.G., Kiser, C.J., Keenan, K.E., Thomas, S.C., 2011. Analysis of osteon morphotype scoring schemes for interpreting load history: evaluation in the chimpanzee femur. *J. Anat.* 218, 480–499.
- Skedros, J.G., Keenan, K.E., Williams, T.J., Kiser, C.J., 2013. Secondary osteon size and collagen/lamellar organization ("osteon morphotypes") are not coupled, but potentially adapt independently for local strain mode or magnitude. *J. Struct. Biol.* 181, 95–107.
- Skedros, J.G., Bloebaum, R.D., Bachus, K.N., Boyce, T.M., Constantz, B., 1993b. Influence of mineral content and composition on graylevels in backscattered electron images of bone. *J. Biomed. Mater. Res.* 27, 57–64.
- Skedros, J.G., Keenan, K.E., Halley, J.A., Knight, A.N., Bloebaum, R.D., 2012. Osteon morphotypes and predominant collagen fiber orientation are adaptations for habitual medial-lateral bending in the human proximal diaphysis: Implications for understanding the etiology of atypical fractures. *58th Annual Meeting of the Orthopaedic Research Society* 37, 1512.
- Sobelman, O.S., Gibeling, J.C., Stover, S.M., Hazelwood, S.J., Yeh, O.C., et al., 2004. Do microcracks decrease or increase fatigue resistance in cortical bone? *J. Biomech.* 37, 1295–1303.
- Sokal, R.R., Rohlf, F.J., 1995. *Biometry. The Principles and Practice of Statistics in Biological Research*, 3rd edition. W.H. Freeman and Co., New York.
- Su, S.C., Skedros, J.G., Bachus, K.N., Bloebaum, R.D., 1999. Loading conditions and cortical bone construction of an artiodactyl calcaneus. *J. Exp. Biol.* 202 (22), 3239–3254.
- Sunny, G., Yuan, F., Prakash, V., Lewandowski, B., 2009. Design of inserts for Split-Hopkinson pressure bar testing of low strain-to-failure materials. *Exp. Mech.* 49, 479–490.
- Vajda, E.G., Skedros, J.G., Bloebaum, R.D., 1998. Errors in quantitative backscattered electron analysis of bone standardized by energy-dispersive X-ray spectrometry. *Scanning* 20, 527–535.
- Vashishth, D., 2004. Rising crack-growth-resistance behavior in cortical bone: implications for toughness measurements. *J. Biomech.* 37, 943–946.
- Vashishth, D., Behiri, J.C., Bonfield, W., 1997. Crack growth resistance in cortical bone: concept of microcrack toughening. *J. Biomech.* 30, 763–769.
- Vashishth, D., Tanner, K.E., Bonfield, W., 2003. Experimental validation of a microcracking-based toughening mechanism for cortical bone. *J. Biomech.* 36, 121–124.
- Vashishth, D., Gibson, G., Kimura, J., Schaffler, M.B., Fyhrie, D.P., 2002. Determination of bone volume by osteocyte population. *Anat. Rec.* 267, 292–295.
- Wang, X., Bank, R.A., TeKoppele, J.M., Agrawal, C.M., 2001. The role of collagen in determining bone mechanical properties. *J. Orthop. Res.* 19, 1021–1026.
- Wang, X., Shen, X., Li, X., Agrawal, C.M., 2002. Age-related changes in the collagen network and toughness of bone. *Bone* 31, 1–7.
- Wasserman, N., Brydges, B., Searles, S., Akkus, O., 2008. In vivo linear microcracks of human femoral cortical bone remain parallel to osteons during aging. *Bone* 43, 856–861.
- Yang, Q.D., Cox, B.N., Nalla, R.K., Ritchie, R.O., 2006. Re-evaluating the toughness of human cortical bone. *Bone* 38, 878–887.
- Yeni, Y.N., Norman, T.L., 2000. Calculation of porosity and osteonal cement line effects on the effective fracture toughness of cortical bone in longitudinal crack growth. *J. Biomed. Mater. Res.* 51, 504–509.
- Yeni, Y.N., Brown, C.U., Wang, Z., Norman, T.L., 1997. The influence of bone morphology on fracture toughness of the human femur and tibia. *Bone* 21, 453–459.
- Zimmermann, E.A., Launey, M.E., Barth, H.D., Ritchie, R.O., 2009. Mixed-mode fracture of human cortical bone. *Biomaterials* 30, 5877–5884.
- Zimmermann, E.A., Schaible, E., Bale, H., Barth, H.D., Tang, S.Y., et al., 2011. Age-related changes in the plasticity and toughness of human cortical bone at multiple length scales. *Proc. Natl. Acad. Sci. USA* 108, 14416–14421.
- Ziopoulos, P., 1999. On microcracks, microcracking, in-vivo, in vitro, in-situ and other issues. *J. Biomech.* 32 (209–211), 213–259.
- Ziopoulos, P., Currey, J.D., 1994. The extent of microcracking and morphology of microcracks in damaged bone. *J. Mater. Sci.* 29, 978–986.
- Ziopoulos, P., Currey, J.D., Sedman, A.J., 1994. An examination of the micromechanics of failure of bone and antler by acoustic emission tests and Laser Scanning Confocal Microscopy. *Med. Eng. Phys.* 16, 203–212.
- Ziopoulos, P., Wang, X.T., Currey, J.D., 1996. Experimental and theoretical quantification of the development of damage in fatigue tests of bone and antler. *J. Biomech.* 29, 989–1002.
- Ziopoulos, P., Currey, J.D., Hamer, A.J., 1999. The role of collagen in the declining mechanical properties of aging human bone. *J. Biomed. Mater. Res.* 45, 108–116.